Editors' Suggestion

Plume-surface interaction during lunar landing using a two-way coupled DSMC-DEM approach

A. Bajpai[1,*] A. Bhateja,[2,†] and R. Kumar[1,‡]

[1]*Department of Aerospace Engineering, Indian Institute of Technology Kanpur, Kanpur 208016, India*

[2]*School of Mechanical Sciences, Indian Institute of Technology Goa, Goa 403401, India*

(Received 21 May 2023; accepted 10 January 2024; published 23 February 2024)

In the present work, a numerical framework is developed for simulating gas-solid flows associated with interaction of a rocket plume on a planetary surface. For this investigation, a unique, two-way coupled, dusty-gas flow model has been developed in the coupled direct simulation Monte Carlo (DSMC)-discrete element method (DEM) framework, which has been applied for dust dispersion on lunar surface. In this model, the gas-gas collisions are modeled probabilistically, whereas grain-grain interactions are computed deterministically. Most importantly, a multiphase fluid-solid two-way coupling model is proposed where the fluid-particle interaction is modeled macroscopically by considering the momentum and energy exchange between the two phases. The use of the DEM approach allows us to model dense granular phase near a planetary regolith. Additionally, the framework allows us to calculate not only the particle trajectories, but also their temperatures. To make the framework efficient for dynamic calculation of drag and heat transfer from gas to grain phase, the same coefficients are precalculated (and used later as a look-up table) for gas flow over an isolated granular particle over a range of speed ratios for free molecular flow conditions. Using the developed framework, a comprehensive numerical study is performed to model dust dispersion associated with lunar landing. The influence of particle diameter on gas and grain phases and dust transportation has been analyzed in the coupled framework. Additionally, the impact of the two-way coupled gas-grain interaction model is analyzed and compared with one-way coupled model.

DOI: 10.1103/PhysRevFluids.9.024306

I. INTRODUCTION

Gas-solid flows are ubiquitous in the natural or industrial world. This can be seen in many different situations, such as fluidized beds, pneumatic transfer, cyclone separation, avalanches, and landslides. The emphasis of this study is on another such scenario: the descent of a spacecraft on a dusty surface, as schematically depicted in Fig. 1. A layer of regolith several meters thick covers the lunar surface. The *Apollo* astronauts noted that lunar dust was one of the primary obstacles for manned missions to the moon. Human operations on the moon disrupt lunar regolith in addition to natural causes, thereby creating dangerous hidden risks [1,2]. When a lander approaches the lunar surface, the expanded supersonic plume from the nozzle exhaust of positioning rockets impinges on the planet's soil or regolith, and interaction between the plume and surface occurs. Due to the moon's near-total vacuum and low gravity, this high-speed and high-temperature plume produces a shock and fluidizes and ejects lunar dust from the surface. Flow-induced pressure creates one or

*aasheesh@iitk.ac.in

†ashish@iitgoa.ac.in

‡Corresponding author: rkm@iitk.ac.in

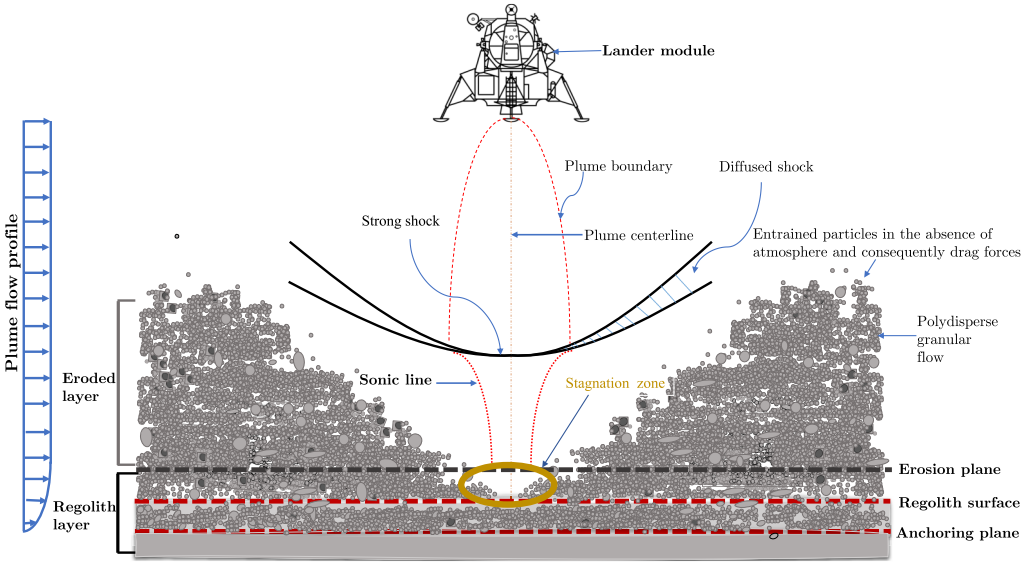

FIG. 1. Illustration of the challenge of lunar landing that classifies distinct regions according to different criteria along with erosion schematic.

more craters by the expulsion of lunar particles. Korzun *et al.* [3] characterized the plume-surface interaction (PSI) using a variety of processes, including erosion, ejecta dynamics, and cratering of planetary regolith. The fluidization of lunar regolith grains caused by the rocket exhaust plume during erosion and ejecta processes has the potential to affect the stability of a landing module. Instruments or astronauts in the area will be seriously impacted from these speeding dust particles, posing a challenge for any lunar mission that relies on soft landing and rocket return. In a recent study by Singh *et al.* [4] at the Indian Space Reserach Organisation, it was determined that an estimated 108.4 m^2 of lunar epi-regolith was covered by uncorrelated "ejecta halo" pixels, which were mapped and classified. These pixels represented lunar epi-regolith ejected as a result of the landing sequence of the *Vikram* lander. Additionally, empirical relations were employed to estimate that approximately 2.06 tonnes of lunar epi-regolith were displaced during the landing event with lander weight of $\sim$1.752 tonnes. Lunar dust was found to deposit on equipment located 17 m from *Apollo 11* and 160 m from *Apollo 12*. Particles were estimated to have traveled at speeds in excess of 100 m/s. Smaller particles suspended during the *Apollo* landings are estimated to have reached escape velocity, posing hazards to orbital hardware. Degradation of thermal control surfaces, dust penetration into the vehicle, damage to solar cells and pressurized vessels, surface obscuration, device clogging, damage to solar cells and pressurized vessels, damaged astronauts' suits and pressurization leaks at 0.25 psi/min, and other issues are related. Studying true physics is necessary for developing mitigation strategies or performing a soft landing on the lunar surface.

The physics and mechanisms were partially discovered through imaging during the landing and experiments. The relatively small number of exploratory missions combined with technological limitations mean that the quantity and quality of data are short of what is needed to study PSI and subsequent dust dispersion. In contrast, some laboratory-scale experiments are repeatable and can provide various high-resolution images at the rates required to potentially model this phenomenon. During the *Surveyor* and *Apollo* eras, studies reported laboratory experiments characterizing granular erosion and crater formation for landing on the moon. Roberts *et al.* [5] did a study for jet impingement, which led to a deterministic model based on the theory that crater formation is governed by the height of the impinging jet and the resulting flow field. Hutton *et al.* [6] used this information and predicted the flow-induced forces from viscous shear stresses on the granular

surface from radial propagation of the exhaust during impingement. This model does not always compare well against data for crater formation and erosion. When comparing to Roberts' theory, Hutton *et al.* [6] stated that "a factor of uncertainty of about 5 for erosion predictions is not excessive." The observed errors led to the model's improvement over the years to account for effects like polydisperse particle phase [6,7]. Land *et al.* [8] presented that after some critical height, the jet did not result in the erosion of granular matter. Alexander *et al.* [9] extended experimental studies, by using a descending rocket nozzle for standard Earth atmospheric conditions. For both vacuum and atmospheric conditions, it was observed that soil properties and flow conditions had a significant effect on crater formation [8,9]. Metzger *et al.* in 2009 [10] and Metzger *et al.* in 2011 [11] combined these works and set the groundwork for recent PSI experiments that aimed to tackle uncertainties in transient crater formation and ejecta phenomena, albeit with some simplifying assumptions. Unfortunately, unless conditions match those experienced during landing, the physics of particle fluidization and ejection can be compromised. To remedy this, Kuhns *et al.* [12] in a recent experiment used a drop tower in combination with a pressurized vessel to study this phenomenon by allowing test cases to mimic conditions for various landing environments. It is difficult to execute accurate studies of plume impingement on granular beds since it is challenging to maintain a vacuum and low-gravity conditions.

The numerical approach is an attractive alternative as it could potentially provide a high-resolution, nonintrusive framework for data collection and model development. In anticipation of the *Apollo* landings, Roberts *et al.* [5,13] began estimating plume impingement on the lunar surface for the *Apollo* missions. Due to the lack of computing resources in the 1960s, ignoring the boundary layer formed on the moon's surface, he studied dust dispersion using an analytical technique by creating the first model for single-engine plume impingement under the assumptions of free molecular, one-dimensional isentropic expansion, one-dimensional normal shock relations, constant drag coefficient for particles, etc. This study determined shear stress, erosion profile, and other surface features as a function of chamber flow variables, thrust, particle diameter, and lander height.

Metzger *et al.* [7] updated Roberts' dust erosion model because it underpredicts the lunar surface dust emission rate. While Gallis *et al.* [14] developed a method to compute local drag and heat transfer on a particle owing to neighboring gas molecules in the direct simulation Monte Carlo (DSMC) framework, they neglected to take into account the effect of solid particles on the gas phase, thus effectively performing a one-way coupled study. Taking inspiration from the work of Gallis *et al.* [14], Gimelshein *et al.* [15] developed a drag model, which is a two-way coupled model, and studied the effect of particles on the gas in the two-way gas-particle coupling implemented in the DSMC framework. This implementation was based on a statistical method to compute deflection angles and employed molecular fluxes to determine the number of gas-particle collisions. As part of this study, they added up the contributions of all the molecules in a given cell to the total heat flux and drag acting on particles. Particles were affected by the gas through gas-particle collisions, and deflection angles were determined using a statistical method. Burt *et al.* [16] expanded Gallis *et al.* [14] to a two-way coupled model by including the impact of particles on gas and investigated unburned alumina particle entrapment in the solid propellant rocket nozzle. In this study, the effect of particles on gas was modeled by taking into account the collision of individual molecules of gas with the particles themselves. Additionally, a Monte Carlo integration technique was used to calculate deflection angles by taking into account both specular and diffuse reflections.

Recently, advancements in numerical simulations of the impinging gas flow field during its expansion from continuous to rarefied flow have allowed for an improvement in the *Apollo* models. The impinging gas flow field in greater thrust descent engines has been simulated using hybrid continuum-kinetic solvers [17,18]. Using flow fields from Lumpkin *et al.* [17] to track particle pathways, Lane *et al.* [19] combined the overlay approach with DSMC to estimate particle properties in a one-way coupled manner. The particle flow field is computed without dust using an overlay approach. This research employed particle sizes ranging from 10 to 500 μm. Therefore, a mathematical model was formulated and subsequently implemented in software. The model's results indicated that

smaller particles attain velocities of ≈ 3 km/s. Marichar *et al.* [18] calculated lunar lander nozzle flows and near-field plume development using a reactive and multiphase method-of-characteristics solver. Consequently, a loosely coupled continuum solver and DSMC analysis algorithm simulated the distant field and plume-surface interaction. Neglecting particle interactions maintained a steady gas phase.

Several hybridization methods have coupled a near-field computational fluid dynamics (CFD) solver with a far-field Boltzmann solver. Tosh *et al.* [20] investigated plume impingement on a flat surface designed to resemble the lunar surface using a hybrid continuum-rarefied CFD solver without considering erosion. The surface shock structure was found to be in excellent agreement between the simulation results and experiments throughout a wide range of background pressure ratios. The two-phase flow was significantly dust-loaded for lunar landing erosion conditions [21]. In order to investigate the dust dispersion that occurs as a result of PSI on a lunar surface, Morris *et al.* [22] used the weakly coupled continuum CFD-DSMC method, and Morris *et al.* [23] used Burt's two-phase model [16] in a hybrid CFD-DSMC solver for lunar landing. The dust erosion profile was empirically generated using *Apollo* landing data to calibrate the dynamic pressure at 5 cm above the lunar surface. There were simulations conducted for various hovering heights, engine thrust, and particle sizes [24]. White *et al.* [25] performed a simulation of plume impingement on a flat surface using the open-source solver `dsmcFoam` without taking into consideration particles and then compared their findings with those predicted by the free molecular theory. The shear stress and heat flow were found to be overpredicted by the free molecular theory. To improve the accuracy of DSMC solvers, a fully coupled two-phase flow model [26] was developed and implemented by Morris *et al.* [22,23,27] and He *et al.* [28]. As the dust slows the gas motion, the total velocity of the dust particles will eventually asymptote towards a lower value when the movements are entirely linked. Berger *et al.* [29] shows that the erosion flux is influenced by particle-particle collisions, which also enhance particle scattering and so modify both the near-field and far-field dust motion [23].

An efficient Eulerian-Eulerian framework was used by Gale *et al.* [30] for the Martian atmosphere, in order to establish a method for adding irregularity of particles that yields experimentally consistent results in comparison to spherical mixtures in the shape of craters on the surface brought about by plume impingement after employing the discrete polydisperse spherical model and discrete element method (DEM). Plume impingement on a flat wall was investigated by Yeager *et al.* [31] using a continuum-based gas-particle model. While the gas phase was treated using the Eulerian framework, the particle phase was studied using the Lagrangian method. In order to take into consideration granular particles in the DSMC framework in a two-way coupled manner, Chinappan *et al.* [32] utilized a modified version of the DSMC framework. In this study, gas-gas collisions were considered using probabilistic Monte Carlo simulations and grain-grain collisions as deterministic, while gas-grain collisions were simulated macroscopically through the estimation of drag and surface heat flux. Recently an open-source solver `dsmcFoamPlus` was used by Cao *et al.* for rarefied vortex loop formation caused by shock wave diffraction around a 90° corner. Agir *et al.* [33] also studied the Edney shock-shock interaction patterns using the same framework. Using this framework, an open-source parallel solver, `rarefiedMultiphaseFoam`, was developed and tested by Cao *et al.* [34] in `OpenFOAM`. The solver is well validated and tested for providing solutions to two-phase rarefied flow problems. This framework was used by Cao *et al.* [35] for solving the PSI problem, in which they considered the scaled-down model of lunar landing to study erosion dynamics on lunar regolith. This type of consideration is expected to result in more accurate erosion modeling and also helps in capturing certain features like crater formation. When looking at the kinetic characteristics of lunar dust, a Lagrangian framework using the discrete phase model was used by Zhang *et al.* [36] for sample analysis of the Chang'e 5 lunar mission.

In order to study PSI, macroscale methods have recently adopted formulations, calledthe Reynolds averaged Navier Stokes (RANS) or large eddy simulation (LES). By employing RANS, one may do numerical simulations of a whole landing site with certain submerged geometries that are approximations of the intended lander or rover [37,38]. These simulations are quite informative since they provide data on the average value of the impinged surface properties, yet the cited

research is often carried out without particles. One of the alternatives is two-fluid LES simulations, which have just been performed for turbulent high-resolution jet impingement on granular beds [39–41]. These researchers used supersonic jets to simulate the environments of Titan [40,41] and Earth [39]. Not only do the models offer qualitative comparisons to the crater creation shown in landing photos [39], but they also include data on particle-fluid coupling, such as contributions of force during the process of crater creation [41]. Rahimi *et al.* [42] used the gas-particle model in the Eulerian-Lagrangian framework to examine plume-plume interactions for a multiple-engine setup. Roberts' erosion model was used to determine how particle properties change as a function of particle size. Another computational framework using the discontinuous Galerkin method was developed for dusty gas flows by Ejtehadi *et al.* [43]. The second-order Boltzmann-Curtiss-based constitutive connection in a two-fluid system of equations was utilized to investigate the lunar dust dispersion issue within this framework. Shallcross *et al.* [44] proposed and used a volume-filtered Eulerian-Lagrangian framework, in combination with an improved immersed boundary method, for modeling two-phase compressible flow associated with jet impingement on flat surfaces and a granular bed. However, the accuracy of the aforementioned two-phase research is yet to be established for the lunar landing problem, since they used continuum-based techniques, which are computationally efficient but may significantly lack in accuracy owing to very high degree of nonequilibrium present.

Rarefied flows or noncontinuum flows, with a high degree of nonequilibrium, are typically studied using the DSMC approach, which is a kinetic particle-based approach and is hence well suited to model the nonequilibrium phenomena at play here. Because of the enormous disparity in the masses of gas molecules and granular particles, the standard collision models that are utilized in the DSMC approach are not suitable to be applied to the study of gas-grain collisions. Therefore, the system has to account for gas-grain collisions and grain-grain collisions differently. Scientific understanding of rocket plume interactions with lunar dust has come a long way since the *Apollo* period. Plume-surface interaction and the resulting dust dispersion can now be modeled, predicted, and analyzed with much better precision. However, the tools that are now available are still not capable of accurately predicting the processes associated with them. Furthermore, for future developments in lunar exploration, it is required to predict distribution of particle velocity, dispersion angles, and trajectories, including defining criteria to mitigate harm to adjacent structures. In this context, the purpose of the present work is to present crucial information on grains/particles ejecting due to plume impingement on lunar surface, such as their trajectories and velocity/angular distribution of ejected particles using a Lagrangian-Lagrangian computational framework, combining particle-based DSMC and DEM approaches for modeling dusty-gas flow dynamics associated with lunar landing. To establish this framework for dusty gas flows, we have integrated an in-house DSMC flow solver with an in-house DEM solver using a two-way coupling approach, thereby allowing for modeling of both dilute and dense granular conditions for PSI, which have not been considered in the literature so far to the best of our knowledge. Using the proposed framework, with ourl gas-grain interaction model for momentum and energy exchange, we can predict not only the velocities/kinetic energies of gas and grain phases, but also their temperature field. Such a solver is not yet available to the best of our knowledge. This kind of information (velocity and temperature for grain phase) can be important for the consideration of spacecraft designers from the standpoint of safety of sensitive electronic surfaces, solar panels, or even the viewpoint of surrounding hardware.

The rest of the paper is organized as follows: in Sec. II, domain description, assumptions, numerical parameters, methodology, erosion modeling, coupling framework, and verification of the model are discussed. Next, in Sec. III, all the simulation results are presented and discussed. After that, in Sec. IV, the key conclusions of the study are presented.

II. COMPUTATIONAL MODELING

Based on the description given about the dust dispersion problems associated with planetary landing, it is clear that experimental setups are extremely expensive and perhaps unrealistic to

TABLE I. Flow regimes based on the Knudsen number [45].

Knudsen number range	Flow regime
$\mathrm{Kn} \leqslant 0.01$	Continuum regime
$0.01 < \mathrm{Kn} \leqslant 0.1$	Slip flow
$0.1 < \mathrm{Kn} \leqslant 10$	Transitional flow
$\mathrm{Kn} \geqslant 10$	Free molecular flow

a certain extent. Therefore, numerical approaches offer an attractive alternative as they could potentially provide a suitable framework for data collection and further model development. The suitability of the framework depends to a large extent on the flow regime, which is classified based on the Knudsen number (Kn) [45] as shown in Table I.

The rocket plume on the moon with a near-vacuum environment will encounter different flow regimes: the gas is in a near-continuum state through the length of the nozzle. As it exits the nozzle, the supersonic plume expands rapidly in both the radial and axial directions, and the flow enters the slip, transition, and eventually free-molecular regime [46]. The PSI problem falls in the transitional and free molecular flow regime. The Navier-Stokes solver is not suitable to study this problem because of continuum breakdown at higher altitudes/rarefied conditions. Therefore, in this work, we have developed a two-dimensional, parallel, multispecies, in-house coupled DSMC-DEM solver to model two-phase dusty-gas flows associated with lunar landing. Both of the solvers have been developed and validated independently. A brief description of the two solvers involved in the computational framework developed in this work is given next.

A. DSMC modeling: Numerical model for the gas-gas interaction

DSMC [46] is a numerical method used to simulate the behavior of dilute gases and plasmas. The DSMC method is typically used to study transitional and free molecular flows. It is a pure simulation method, which provides a physics-based solution to the Boltzmann equation by mimicking the behavior of the molecules. It is based on the kinetic theory of gases, where the motion of individual molecules is tracked in a simulation. DSMC is particularly useful for simulating rarefied gases, where the mean-free path of the molecules is large compared to the size of the system being simulated. This technique works with simulated molecules, each of which represents a substantial number of actual molecules. This approach bases physics on the motions and collisions of molecules. This strategy relies on isolating the effects of molecular motion from those of collisions between molecules. The motion of the molecules is treated in a deterministic manner, but the collisions between the molecules are modeled probabilistically. The size of the cell should be less than the gas's mean-free path, while the time step should be much less than the average collision time. The temporal and/or ensemble average of the data is used to derive macroscopic properties. In this study, an in-house DSMC solver known as the nonequilibrium flow solver (NFS) has been used and further updated to develop DSMC-DEM solver. Figure 2(a) shows a complete flowchart of the methodology used in the NFS framework. Elastic collisions in the NFS are modeled using the variable hard sphere model. To determine the total number of collisions at a given time step and number density in a specific cell, Bird's no-time counter approach is used. Inelastic collisions can be modeled using the quantum and continuous Larsen-Borgnakke models. The Cercignani-Lampis-Lord [47] or the Maxwell model [48] was used to analyze gas-surface interactions. The 2D NFS solver is made parallel in the MPI framework. The solution was tested using a variety of case studies to ensure its accuracy [49,50]. In the current work, the same solver is utilized for simulating gas-gas interactions. All the gas simulations like continuum flow within the nozzle, gas-impingement on the lunar surface, and far-field simulation have been simulated using the same. In this work, we have simulated an engine analogous to the lunar module descent engine

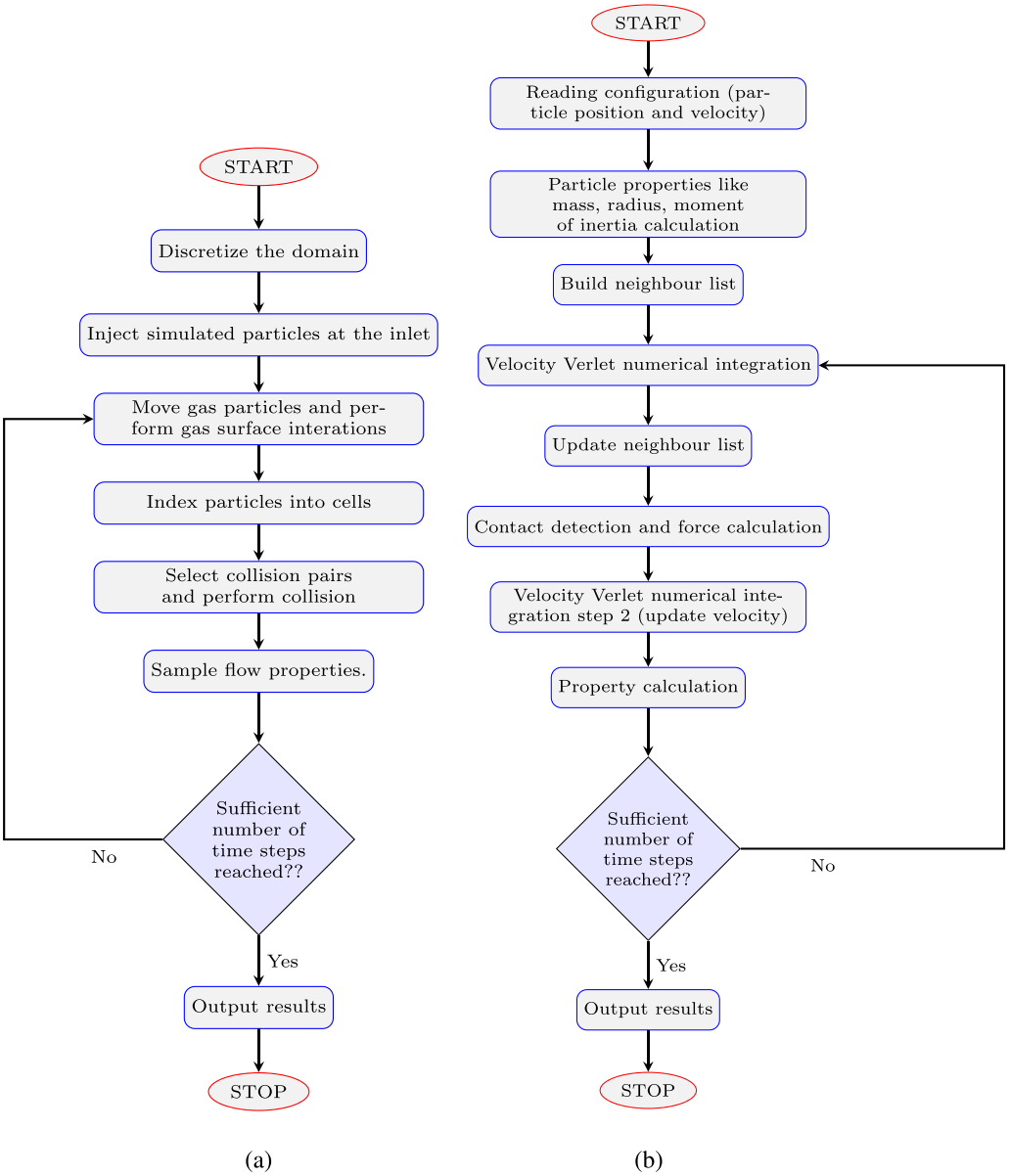

FIG. 2. Gas and grain simulation methodology. (a) DSMC method flowchart; (b) flowchart of DEM used.

(LMDE), which enables direct comparison to *Apollo* landing measurements. The working fluid used in this work is water vapor.

B. Numerical model for grain-grain interaction: DEM modeling

The primary goal of discrete element method (DEM) is to produce particle trajectories by numerically integrating the equations of motion in order to compute different attributes of interest. In the DEM individual objects interact along their boundaries. The contact between two particles is modeled using various interaction laws [51–53]. A typical force law uses a spring and dashpot,

where the particle elasticity and collisional dissipation are described by the spring stiffness and the damping coefficient, respectively. The deformation is considered in terms of the overlap between particles, which is used to compute elastic and frictional forces between particles. The contact forces change with time during a collision. Particle motion is governed by Newton's second law. For spherical particles, the equations of motion may be written as

$$m_i \frac{\mathrm{d}\boldsymbol{v}_i}{\mathrm{d}t} = m_i \frac{\mathrm{d}^2\boldsymbol{x}_i}{\mathrm{d}t^2} = \sum_{CL} \left(\boldsymbol{F}_n^{ij} + \boldsymbol{F}_t^{ij}\right) + \boldsymbol{F}^{\mathrm{ext}}, \tag{1}$$

$$I_i \frac{\mathrm{d}\boldsymbol{\omega}_i}{\mathrm{d}t} = \sum_{CL} \boldsymbol{M}_t^{ij}, \tag{2}$$

where i stands for the identifier of a particle, m_i is the mass of that particle, CL refers to the contact list associated with the particle i, I_i is the moment of inertia of particle i, $\boldsymbol{v}_i$ and $\boldsymbol{\omega}_i$ are the particle's linear and angular velocities, respectively, $\boldsymbol{x}_i$ represents the location of particle i, and j iteratively considers all particles that are included in the ith particle contact list. The first term on the right-hand side (r.h.s.) of Eq. (1) is the sum of the normal ($\boldsymbol{F}_n^{ij}$) and tangential ($\boldsymbol{F}_t^{ij}$) contact forces acting on the particle i due to its interaction with particle j. The term $\boldsymbol{F}^{\mathrm{ext}}$ refers to the external forces, such as gravitational force, electromagnetic force, and fluid-particle interaction forces. The torque $\boldsymbol{M}^{ij}$ acts on particle i due to the tangential force $\boldsymbol{F}_t^{ij}$ exerted by particle j.

The DEM has three primary steps: (1) searching particles for potential contacts, (2) force calculation, and (3) updating the location and velocity of particles. The algorithm used for this framework is described in Fig. 2(b). This study employs the linear spring-dashpot (LSD) model for particle-particle interactions. Particles are assumed to be spherical, dry, and cohesionless. The friction between particles is incorporated utilizing the Coulomb friction criterion [52–54]. The equations of motion are integrated numerically using the velocity Verlet integration approach [55]. Further details of the simulation scheme can be found elsewhere [56]. The stability of the scheme is determined by the magnitude of time step δt, which is a fraction of the time period of an undamped spring-mass system [57].

C. Numerical model for gas-grain interactions: Interaction between flow field and moving particles

Due to the considerable disparity in mass and diameter between gas and granular particles, the numerical modeling of real gas-grain binary collision in the DSMC framework is exceedingly difficult [50]. Furthermore, carrying out surface-resolved analysis to obtain forces due to fluid phase on a particle is quite expensive. Therefore, forces and heat transfer between fluid and granular particle are obtained following our own approach. As part of this approach, aerodynamic (drag) and heat transfer coefficients are computed for a single isolated granular particle by considering gas flow over it in a separate simulation. As the flow conditions over a granular particle correspond to highly rarefied or nearly free molecular regime due to its small size and low gas density conditions (especially true away and radially outward from the nozzle), a modified in-house DSMC solver, tuned to work efficiently in free molecular flow conditions, is employed to obtain such coefficients over a single isolated grain over a range of speed ratios [58]. This simplifying assumption of considering flow over an isolated grain has been adopted to ease the modeling of gas-grain interactions. This implicitly assumes that the interparticle spacing, on average, is much larger than the particle diameter, or in other words particles are not nearly touching. The validity of this assumption can be verified by relating particle volume fraction to interparticle spacing, l, and particle diameter, d, as follows [59]:

$$\frac{l}{d} = \left(\frac{\pi}{6\alpha_d}\right)^{1/3}. \tag{3}$$

Since the volume fraction within the problem domain remains below 0.1%, the l/d ratio consistently exceeds 8.06. This indicates that interparticle spacing or the distance between two grains always surpasses this value. This justifies our assumption of considering drag and heat transfer coefficients

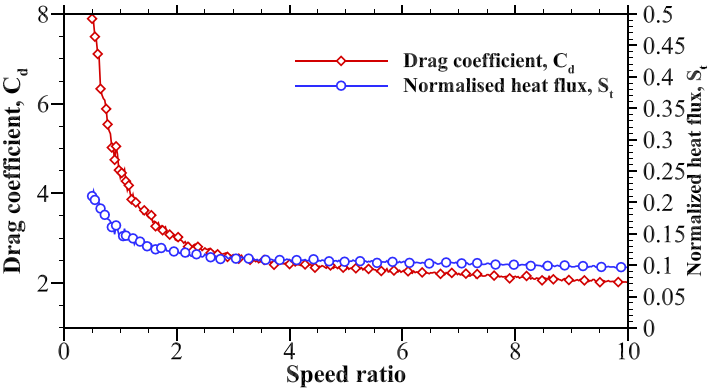

FIG. 3. Normalized heat flux and coefficient of drag variations with speed ratio.

over a single isolated particle for the entire domain. Furthermore, as particles move further/radially outward, it becomes evident that there would be an increasing degree of rarefaction, wherein the Knudsen number may be much larger than 10, thereby justifying the use of free molecular flow assumption.

The drag and heat transfer coefficients, calculated in the above-mentioned manner, are tabulated and then used as a look-up table to interpolate the values of these coefficients dynamically for any interaction of a granular particle with its surrounding fluid at a given cell and time step, i.e., corresponding to a specific relative speed ratio. This is how the momentum and energy exchange between the two phases are effectively carried out to compute drag force, convective heat transfer, and skin friction heating. The values of the drag coefficient (C_D), and the Stanton number (St_n), for a range of speed ratios are shown in Fig. 3, and the same is saved in the form of a look-up table. The interaction between the flow field and moving particles are treated by interpolation, which requires values from the table to compute the drag (D) that a particle experiences, as well as the convective heat transfer rate from the gas to the particle. For example, flow over a sphere of diameter 1μm (granular particle size) is simulated at different speed ratios from 0 to 10 with a difference of 0.1 to obtain drag coefficient and Stanton number. Now, C_D and St_n can be found for any local cell-based speed ratio using interpolation from the look-up table. This modeling methodology is adopted from Chinnappan *et al.* [32].

1. Gas-grain interaction: Effect of gas phase on grain

Drag, D, and the convective heat transfer rate, Q_{conv}, of granular particles in each cell are calculated using the look-up table values for the drag coefficient and the Stanton number:

$$D = \tfrac{1}{2}\rho_c v_r^2 A_p C_D, \tag{4}$$

$$Q_{\mathrm{conv}} = \rho_c |v_r| C_{p,\mathrm{gas}} (T_{aw} - T_p) A_p \mathrm{St}_n, \tag{5}$$

where D represents the amount of drag that a particle is subjected to, Q_{conv} is the gas-to-particle convective heat transfer, ρ_c is the local gas density within a particular cell, $C_{p,\mathrm{gas}}$ is the specific heat capacity of gas, $|v_r|$ is the magnitude of the relative velocity between a granular particle and the local bulk velocity of gas, A_p represents the cross-sectional area of a granular particle, T_{aw} is adiabatic wall temperature corresponding to the local gas temperature and relative velocity magnitude v_r, and m_p and T_p are the mass and temperature of a granular particle. Using the values of drag and

convective heat transfer rate, as given by Eqs. (4) and (5), the velocity and temperature of granular particle are updated as

$$\mathbf{V}_p^{t+1} = \mathbf{V}_p^t - \frac{D\Delta t}{m_p}\frac{\mathbf{V}_r}{|\mathbf{V}_r|}, \tag{6}$$

$$T_p^{t+1} = T_p^t + \frac{Q_{\text{conv}}\Delta t}{C_{p,p}m_p}, \tag{7}$$

where V_p, m_p, and $C_{p,p}$ are velocity, mass, and specific heat capacity of a granular particle, $\mathbf{V}_r$ is the relative velocity vector between a granular particle velocity, V_p and local bulk velocity of gas, $\mathbf{U}$, i.e., $\mathbf{V}_r = \mathbf{V}_p - \mathbf{U}$, Δt is the time step associated with the DSMC method.

2. Gas-grain interaction: Effect of grain on gas phase

The impact that granular particles have on the gas phase is analyzed with regard to momentum and heat exchange, as was explained before. The energy that is lost as a result of interactions between grains and gas grains is turned into heat, which causes a rise in the temperature of a cell locally. We use the energy gain or loss in a collisional cell to increase or decrease the local thermal motion of gas molecules, respectively, according to the heat accommodation model proposed by Kumar *et al.* [60]. Energy-conserving properties of this model were verified by [60], and in the next section, model has been validated along with momentum conservation. According to this model, the heat accommodation factor is given as

$$\phi = \sqrt{\frac{E_{tr} + \dot{Q}\Delta t}{E_{tr}}}, \tag{8}$$

where the total random translational energy in a cell, E_{tr}, is given by

$$E_{tr} = \sum_{i=1}^{3}\sum_{n=1}^{N}\frac{1}{2}m(u_{i,n} - U_i)^2, \tag{9}$$

where $u_{i,n}$ represents the velocity of the nth simulated gas molecule in the ith direction, U_i represents bulk velocity of gas in the ith direction, N_g represents total number of simulated gas molecules in a cell, and m_n represents mass of an nth simulated gas molecule.

The total amount of energy that is lost to gas in one unit of time, Q, is equal to

$$\dot{Q} = (\dot{Q}_{gr-gr} + \dot{Q}_{\text{gas}-gr}) = (\dot{Q}_{gr-gr} + \dot{Q}_{\text{conv}} + \dot{Q}_{sf}). \tag{10}$$

The energy loss per unit time in grain-grain interactions, Q_{gr-gr}, is the difference in relative kinetic energy before and after a collision. Thus, it depends on the coefficient of friction and coefficient of restitution considering the grains to be rough and inelastic. Here the rate of skin-friction heating, denoted by the symbol $\dot{Q}_{sf}$, is expressed as

$$\dot{Q}_{sf} = D\left(\mathbf{V}_r \cdot \frac{\mathbf{V}_r}{|\mathbf{V}_r|}\right). \tag{11}$$

Using the heat-accommodation model [60], the velocity of gas molecules in a cell is altered in the following manner:

$$u_i' = \underbrace{\phi(u_i - U_i)}_{\text{Energy conservation}} + \underbrace{(U_i + \delta U_i)}_{\text{Momentum conservation}}, \tag{12}$$

where u_i' is the new gas particle velocity (in the ith direction) due to momentum and energy exchange with the grain phase, u_i stands for the x, y, and z components of the velocity of a gas molecule, and U_i stands for the x, y, and z parts of the bulk velocity of the gas. The first term of the r.h.s. of Eq. (12) represents the change in the thermal velocity of gas molecules due to energy exchange with grain

phase locally. On the other hand, the second term on the r.h.s. represents the change in bulk velocity due to local momentum exchange with gas phase. The change in bulk velocity, ($\delta\mathbf{U}$), of gas due to momentum change is given by

$$\delta\mathbf{U} = \frac{D}{N_g F_g m_g} \frac{\mathbf{V}_r}{|\mathbf{V}_r|} \Delta t, \tag{13}$$

where N_g is the total number of gas molecules in a cell, F_g is the number of real molecules that a single simulated molecule represents, and m_g is the mass of a gas molecule. Taking into account the change in bulk velocity caused by the exchange of momentum with the granular phase, the final equation for changing the speed of gas molecules is given in Eq. (13). Now we shall discuss the verification of the gas-grain interaction model employed in this work.

D. Verification of gas-grain interaction model

Verification has been performed on the two-way coupled gas-granular solver for an unsteady situation. The relaxation of a particle's velocity and temperature when it comes into contact with a gas, as well as the simultaneous relaxation of gas with a particle, is investigated and then compared with the results of an analytical model (as discussed below). The verification has been done by comparing the analytical results to the simulation results obtained by employing gas-grain interaction model for a single cell. Thus, the simulation can be called zero-dimensional, which efficiently allows us to compare the gas-grain interaction model with theory. As part of this verification process, the relaxation of a spherical grain particle to gas conditions and vice versa has been taken into account. The two-way coupled model is used to account for momentum and heat exchange between the gas and granular phase; therefore the grain's velocity and temperature are set to be different from the gas. Using a two-way coupled technique, as described in Sec. II C, we have investigated the gas-grain interaction and its effect on the particle's velocity and temperature, and these results have been compared with analytical results.

Noteworthy is the fact that the theory does not account for grain-grain interactions, and therefore it is applicable to dilute granular flows only, wherein grain-grain interactions can be ignored. In an attempt to make a fair comparison with the theory, we did not consider grain-grain interactions, and hence kinetic energy loss associated with it, in our simulations. To achieve this, we have just considered a single particle relaxing in a gas. The following are the governing equations for a dusty-gas flow, assuming uniform gas characteristics.

1. Analytical relations

In this section we give the equations for the analytical relations as follows:
the equation for momentum in the gas phase:

$$m_g \frac{d\mathbf{V}_g}{dt} = \mathbf{F}_g, \tag{14}$$

the momentum equation for the grain phase:

$$m_p \frac{d\mathbf{V}_p}{dt} = \mathbf{F}_p, \tag{15}$$

the equation for thermal energy in the gas phase:

$$m_g \frac{de_g}{dt} = Q_{\mathrm{conv}_{gr-gas}} + \mathbf{F}_g \cdot (\mathbf{V}_p - \mathbf{V}_g), \tag{16}$$

and the equation for thermal energy in the grain phase:

$$m_p \frac{de_p}{dt} = Q_{\mathrm{conv}_{\mathrm{gas}-gr}}, \tag{17}$$

where g and p stand for gas phase and grain phase, respectively. Mass in the gas phase is denoted by m_g, whereas mass in the grain phase is denoted by m_p. The gas velocity is denoted by $\mathbf{V}_g$, whereas the grain particle velocity is denoted by $\mathbf{V}_p$, the internal energy of a gas, denoted by e_g, and grain particle, denoted by e_p. For the gas phase, the force is denoted by F_g, and for the grain phase, force is denoted by F_p, which has the same magnitude as F_g but is in the opposite direction, i.e., $F_p = -F_g$. Conversely, $Q_{\text{conv}_{gr-\text{gas}}}$ is the rate of convective heat transfer from the grain phase to the gas phase, and $Q_{\text{conv}_{\text{gas}-gr}}$ is the rate of convective heat transfer from the gas phase back to the particle, such that $Q_{\text{conv}_{gr-\text{gas}}} = -Q_{\text{conv}_{\text{gas}-gr}}$. Thus, our model is capable of predicting not just the velocity (and hence trajectory) of particles ejected, but also their temperature field. This is a unique capability associated with our planetary landing model.

An additional term is added to the thermal energy of the gas phase that accounts for frictional heating and dissipation; it is the second component on the r.h.s. of Eq. (16). Notable is the fact that the work caused by gaseous drag on particles affects solely their kinetic energy in bulk [61], and this means that the only way thermal energy of granular particles could vary is through the transfer of heat to or from it, as given in Eq. (17). Using the theoretical formulations (provided below) in terms of the drag coefficient and the modified Stanton number, the drag force experienced by a particle and the convective heat transfer rate for the aforementioned governing equations are calculated. In the domain of free molecular flow, the coefficients of particle drag and heat transfer rely simply on the molecular speed ratio [62,63]. In the case of free molecular flow, the analytical relationship for the drag coefficient of a spherical granular particle [62] is provided by the expression

$$C_D = \frac{e^{S^{1/2}}}{\sqrt{\pi}S^2}(1+2S^2) + \frac{4S^4+4S^2-1}{2S^4}\text{erf}(S) + \frac{2\sqrt{\pi}}{3S_w}. \tag{18}$$

The drag force that a particle experiences, denoted by the equation $D = -F_p$, may be calculated by putting the drag coefficient [Eq. (18)] into the drag [Eq. (4)]. The rate of heat transfer by convection from a gas to a spherical grain particle is denoted by the notation $Q_{\text{conv}_{\text{gas}-gr}}$ [64]. This rate is represented in terms of the thermal recovery factor, r', and the modified Stanton number, St', as shown in the following equation:

$$Q_{\text{conv}_{\text{gas}-gr}} = \rho_{\text{gas}}|v_r|C_{p,gas}(T_r - T_p)A_p\text{St}'\frac{\gamma}{\sigma'(\gamma+1)}, \tag{19}$$

where ρ_{gas} is gas density, $|v_r|$ is the magnitude of relative velocity between a granular particle and bulk gas velocity, γ is the gas-specific heat ratio, and σ' is the accommodation coefficient, which is taken as unity for this study (fully diffuse condition). The modified Stanton number, St', is given as follows:

$$\text{St}' = \frac{S^2 + S\,\text{ierfc(S)} + \frac{\text{erf}(S)}{2}}{8S^2}, \tag{20}$$

where the integrated complementary error function is denoted by the operator name $\text{ierfc}(S)$. The recovery gas temperature, T_r, in Eq. (19), is calculated from gas temperature, T_{gas}, and total temperature, $T_{o_{\text{gas}}}$, as follows [63]:

$$T_r = T_{\text{gas}} + r'(T_{o_{\text{gas}}} - T_{\text{gas}})\frac{\gamma}{\gamma+1}. \tag{21}$$

Here the thermal recovery factor, denoted by r', is calculated by following equation:

$$r' = \frac{(2S^2+1)\left[1+\frac{\text{ierf}(S)}{S}\right] + \frac{2S^2-1}{2S^2}\text{erf}(S)}{S^2\left[1+\frac{\text{ierfc}(S)}{S}\right] + \frac{\text{erf}(S)}{2S^2}}. \tag{22}$$

Since the gas and grain phases are constantly exchanging momentum and energy, it is important to constantly update the velocities and thermal energies (temperature). Equations (14)–(17) are solved in conjunction with Eqs. (18)–(22).

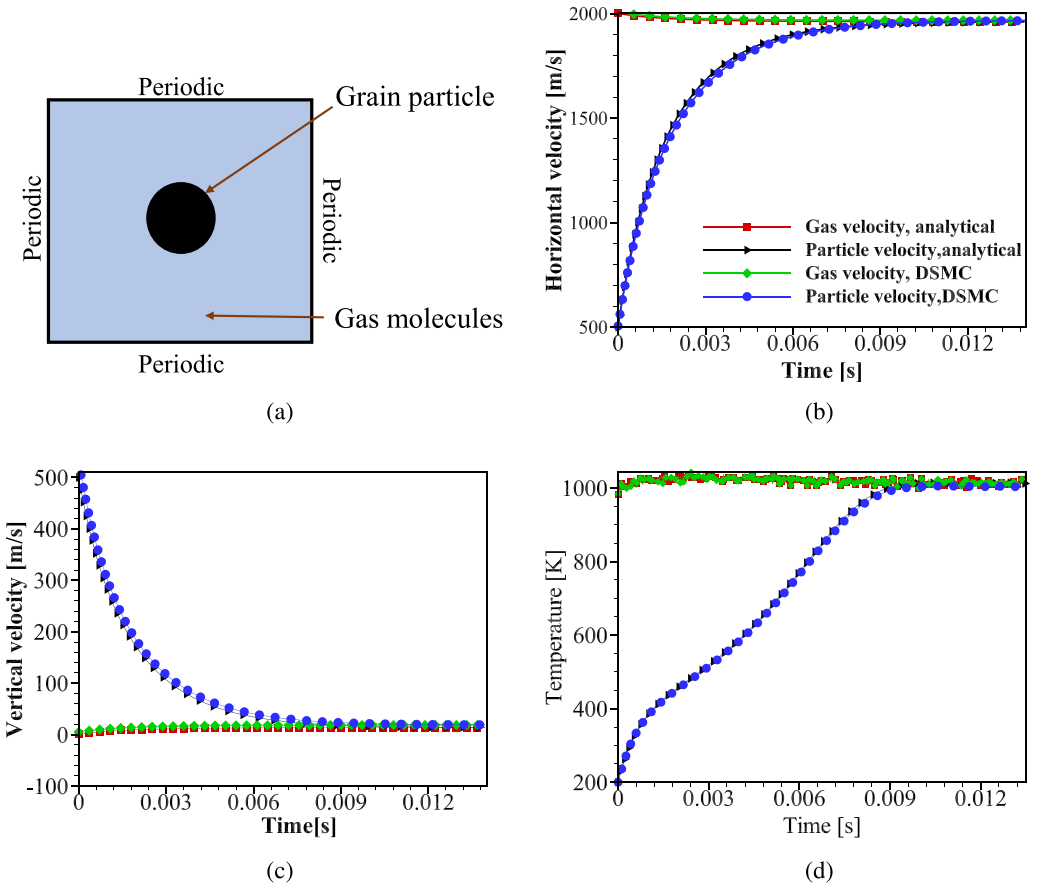

FIG. 4. Verification parameters: (a) domain of verification, (b) horizontal velocity, (c) vertical velocity, and (d) temperature variation.

2. Comparison of numerical results with analytical results

A rectangular domain of size 10×10 μm has been considered for this verification, as shown in Fig. 4(a). Given that the domain dimensions are substantially less than the mean-free path, λ, of the gas, no computing grid is employed in this simulation for the domain. In order to ensure that the case study is in line with the theory, the periodic boundary condition is applied to all four sides of the domain. For the simulations, nitrogen is considered as the gas. An unsteady simulation is carried out using 10 000 simulated gas molecules and one granular particle. The initial horizontal component of gas velocity is taken as 2000 m/s, and the vertical component of gas velocity is taken as 0 m/s. It is assumed that the starting grain velocity is equal to 500 m/s in both directions. It is assumed that the gas number density is $8\times10^{21}(1/\mathrm{m}^3)$ and the number density of grain phase is $1\times10^{10}(1/\mathrm{m}^3)$, which corresponds to the dust to the gas mass fraction of 0.026. Initially, the temperature of the gas and the grain is set to 1000 and 200 K, respectively. The grain particle is assumed to have a diameter of 1 μm and a mass of 9.95×10^{-16} kg. The time step is considered to be 2×10^{-9} s, which is substantially less than the mean collision time of the gas. Properties of the gas and the granular particles are updated at each time step. In Figs. 4(b)–4(d), the theoretical predictions are presented with the temporal variations of velocity components and temperature. The granular particle's y momentum is effectively transmitted to the molecules of gas, while the gas's energy and x momentum are transferred to the particle. The results of the DSMC simulations can be found to be in excellent agreement with the theory [61].

E. Surface erosion mechanism: Lunar surface erosion model

On the basis of the experimental analysis conducted at the Mauna Kea lunar test site, Metzger *et al.* [11] classified three probable erosion processes applicable to planetary landings: bearing capacity failure (if impingement pressure exceeds the bearing strength of the soil), dispersed gas erosion (gas driven through porous spaces), and viscous erosion (if surface shear exceeds the cohesive strength of the soil). The results concluded that viscous erosion is the predominant erosion mechanism on the lunar surface due to low porosity, high packing density, and high bearing strength of lunar soil. *Apollo* landing videos and photographs showed [65] that the crater depth is not very large, and dust propagated more in the radial direction. When shear stress on the surface causes the top layer of loose particles to roll, viscous erosion occurs. The typical viscous erosion equation can be written as

$$\dot{m} = \alpha'(\tau - \tau_{cs}), \tag{23}$$

where $\dot{m}$ is the mass flux of soil ($\frac{\text{kg}}{\text{m}^2\,\text{s}}$), α' is erosion coefficient that has units of s/m, τ is the applied shear stress, and τ_{cs} is the cohesive strength of the soil. This equation is valid only if τ is greater than τ_{cs}, and the mass flow rate is zero for τ less than or equal to τ_{cs}. Modeling of cohesive strength for lunar particles is highly complex due to lack of data about particle geometry and interaction forces. Roberts [5] attempted to include the cohesion effects by defining a threshold shear stress, τ_c, below which the erosion does not occur and proposed an equation to calculate erosion flux along the lunar surface as

$$\dot{m} = \frac{2}{au}(\tau - \tau_c), \tag{24}$$

where au is the fraction of velocity that a dust particle obtains $0 < a \leqslant 1$, and τ_c threshold shear stress. The threshold shear stress is given as

$$\tau_c = c + P\ \tan\phi, \tag{25}$$

where c denotes cohesive stress, P denotes the static pressure of gas at the surface, and ϕ denotes angle of repose of the soil. The above equation reported by Roberts *et al.* [5,66] underpredicts the erosion when compared to *Apollo* landings [67]. Through several experimental studies, Metzger [11,67] improved the Roberts model and found the proportionality of erosion equation with fluid shear stress. In one of the recent studies performed by the same group, the erosion equation is given as [68]

$$\dot{m} = K(\tau - \tau_c)^{\beta}, \tag{26}$$

where K is a constant coefficient, and β is another constant, which is unity for the Roberts model. Moreover, the same study [68] resulted in the formulation of an equation based on the *Apollo* data for total erosion rate, $\dot{M}$(kg/s), with respect to the hovering altitude, h, given as follows:

$$\dot{M} = 2.2e^{-309h}, \tag{27}$$

where h is the hovering altitude. Equation (27) can be used to find the total erosion rate at a particular hovering altitude/impingement height; however, it cannot be used to find the variation of mass flow rate, $\dot{m}$, along the lunar surface. The erosion flux has been determined using Eq. (26) for this study. We verify that the overall erosion rate provided by the constant coefficient, β, computed at particular altitudes agrees with the *Apollo* measurements, given by Eq. (27). The dynamic pressure applied by gas, P_d is given as

$$P_d = 0.5\rho V^2, \tag{28}$$

where ρ is the density of the gas and V is the velocity. Numerous investigations [21,23] show that gas dynamic pressure is directly related to erosion flux; so the dynamic pressure assessed above the macroscopic roughness of the lunar surface (at 10 cm) is employed as applied shear stress, τ, in the erosion equation. The (dynamic) pressure field that is produced by the rocket plume amplifies

the forces that are operating perpendicular to the lunar surface, which ultimately results in surface regolith erosion through a variety of processes. The pressure field is an important parameter to consider in order to have an understanding of how the soil may be able to withstand such dispersed loads and which parts are more likely to be impacted. The plume's impact on the lunar surface results in viscous erosion, which in turn causes granules to be ejected. Particle flow from the surface is determined using the erosion equation (26), as explained earlier. Section III displays the dynamic pressure, which is proportional to the shift in erosion flux on the lunar surface. There it is observed that fluctuation in erosion flow is due to a change in dynamic pressure in the radial direction from the plume's central axis. Notable is the fact that precise erosion modeling is not the focus of attention in this work, but rather the modeling of the movement/dispersion of dusty gases is the key aspect studied in this work. However, in Sec. III, the suggested erosion equation, which is Eq. (26), is evaluated and compared in light of the data obtained from earlier lunar exploration missions.

F. Coupling algorithm

The flowchart of the coupling algorithm associated with multiphase DSMC-DEM solver is presented in Fig. 5. First, the domain is described and discretized according to the mean-free path. Then the physical properties of rocket plume and lunar particles are provided for the simulation. Using this, a DSMC simulation of plume (water vapor) flow through the nozzle is performed, and baseline properties are extracted from nozzle exit. The average baseline properties like values of density, velocity, and temperature are then supplied to the next stage DSMC simulation. The flow field is obtained by the first DSMC subcycle in which only high-speed plume impinging on a flat lunar surface is simulated. After obtaining the flow field, this is transferred to the coupled framework where the calculation of the number of particles eroded at each time step is performed according to dynamic pressure applied on the surface. This information acts as initial conditions for DEM subcycles, and the flow field is first evolved according to the boundary conditions considering momentum and energy transfer between the plume and lunar particles (particle-fluid interaction forces). Hereafter, lunar particles are allowed to move in the plume background. The forces acting on the lunar particles are then calculated and applied. With the hydrodynamic forces and particle-particle contacting forces, the information of particle motions in terms of accelerations, velocities, and positions are calculated and updated. This will provide information about the lunar particle flow field, which also supplies momentum and energy transfer from lunar particles to plume in a two-way coupling approach, and the DSMC cycle is again run to calculate the effect of particles on gas. This completes the loop. With the updated gas flow field, the particle flow field again can be updated. Finally, all the macroscopic properties can be evaluated at the next time step.

G. Properties of lunar dust particles

All the parameters used in the simulations performed in this work are provided in Table II.

In this work particles with different diameter are used based on the particle size distribution. Particle size distribution for lunar regolith has been measured and reported in Carrier *et al.* [69]. Table III lists the maximum number of eroded particles for different particle diameters utilized in this work. It is computationally prohibitive to use particle sizes less than 50 μm, and therefore in this work we have considered only particle sizes above 50 μm. As the diameter of eroded lunar particles decreases, the total number of particles within the simulation domain increases (as given in Table III). This surge in particle count leads to a significant/prohibitive slowdown of DEM computations. To add to this, as particle size decreases, the integration time step size must be reduced, which collectively extends the time required to execute these simulations to a considerable extent. Furthermore, it is crucial to note that, as we decrease the particle diameter below $\sim 50/100$ μm, the consideration of cohesive forces becomes increasingly significant, which is not considered in our model. Because the movements of the gas and dust are fully coupled, we select a set of discrete particle sizes that best resolve the particle mass distribution. In this work, lunar soil

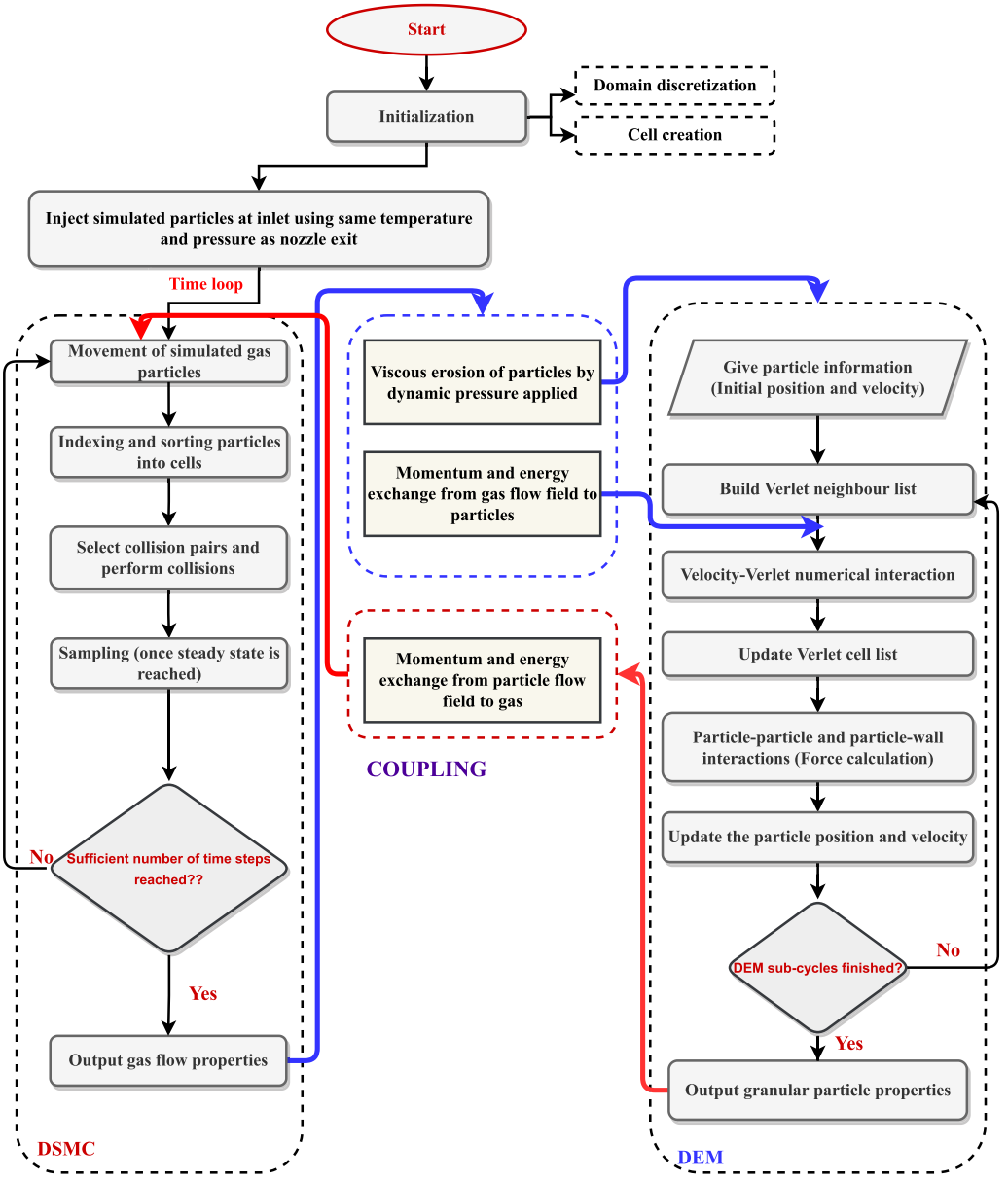

FIG. 5. Flowchart representing the DSMC-DEM coupling algorithm.

particles are depicted as spheres, although the actual particle shape is jagged, spiky, uneven, and rough. The corrected density ρ_p, which accounts for irregular particle shapes, is the ratio of the particle mass to the volume of a sphere of the equivalent aerodynamic cross section. The parameters used and the maximum number of particles eroded are shown in Table III.

H. Domain description

To simulate plume jet flow in the lunar environment, we have used a single rocket nozzle with its nozzle exit perpendicular to a flat surface. Figure 1 shows the representation of a powered landing scenario. We could take into consideration only an axisymmetric plane due to the symmetry of the

TABLE II. Simulation parameters [29].

Particle properties	
Diameter, d	100 μm to 5 mm
Density, ρ	2700 kg/m^3
Time step (min), Δt	1.41×10^{-9} s
Maximum no. of particles, n	600 000
Plume properties	
Number density	2.34×10^{22} m^{-3}
Temperature	1000 K
Velocity	3048 m/s
Particle collision properties	
Spring stiffness	
Particle-particle [Normal], $k_{\text{norm},pp}$	8000 kg/s^2
Particle-particle [Tangential], $k_{\text{tan},pp}$	8000 kg/s^2
Particle-wall [Normal], $k_{\text{norm},pw}$	8000 kg/s^2
Particle-wall [Tangential], $k_{\text{tan},pw}$	8000 kg/s^2
Friction coefficient	
Particle-particle, $\mu_{\text{norm},pw}$	0.20
Particle-wall $\mu_{\text{tan},pw}$	0.20
Coefficient of restitution	
Particle-particle, $e_{\text{norm},pw}$	0.80
Particle-wall $e_{\text{tan},pw}$	0.80
Dashpot coefficient	
Particle-particle, $e_{\text{norm},pw}$	0.80
Particle-wall $e_{\text{tan},pw}$	0.80
System geometry	
Distance from impingement point	4 m
Erosion zone length	10 m
Total domain length	35 m

problem. The physical model diagram is shown in Fig. 6, along with the dimensions and boundary conditions related to each surface. The rocket's plume strikes with the surface of the ground, which is presumed to be impenetrable. Due to the near-vacuum, gas expands in all directions, lowering density and increasing velocity, creating shock waves that interact with the bottom surface and surroundings. The boundary conditions for the gas flow are as follows:

Bottom wall: The wall, having a surface accommodation coefficient equal to one, is presupposed to exhibit diffuse reflection of gas particles from a surface, with full thermal accommodation. This condition maintains a constant temperature equal to 200 K, which is the average lunar soil temperature; symmetry plane: symmetry condition; and outlet surfaces: vacuum condition.

TABLE III. Different diameter particle and their corresponding mass, time step calculated for simulation and maximum number of eroded particles.

Diameter [m]	Mass [kg]	Time step [s]	Maximum no. of particles eroded
5×10^{-3}	1.76×10^{-4}	2.5×10^{-5}	17 370
4×10^{-3}	9.05×10^{-5}	1.69×10^{-5}	29 295
2×10^{-3}	1.13×10^{-5}	6.0×10^{-6}	146 665
1×10^{-3}	1.41×10^{-6}	2.11×10^{-6}	225 047
5×10^{-4}	1.76×10^{-7}	7.46×10^{-7}	325 078
1×10^{-4}	1.41×10^{-9}	6.68×10^{-8}	585 677

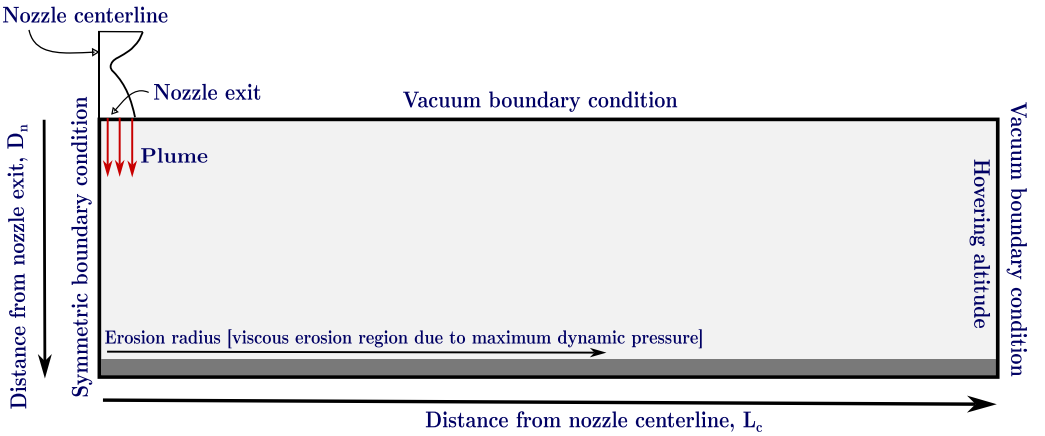

FIG. 6. Schematic view of plume impingement on a lunar surface.

After the gas flow is solved, the trajectories of the ejected lunar soil particles may be determined (using the method outlined in the previous section and in Sec. II J) by considering the momentum and energy transfer between two phases, which is responsible for drag force. Lunar gravity also contributes to particles movement. The mass of a particle multiplied by the acceleration of gravity due to the moon (1.62 m/s^2) gives the particle's weight. The drag force is directly proportional to the drag coefficient, which can be determined through the empirical drag coefficient, which is precalculated at different speed ratios in this work. There is a complete elastic rebound when a particle collides with any surface other than outlet surfaces. Upon reaching the end solution time or upon a particle leaving the domain through outlet surfaces, the single-particle trajectory simulation terminates.

I. Assumptions and approximations for the simulations

The key assumptions made in performing the analysis in this work are as follows:

(1) Particle (grain) phase is monodisperse and the particles are considered spherical in shape.

(2) Particles are not subject to Brownian forces due to their interaction with gas phase.

(3) The surface of the moon is perfectly flat, and the only type of erosion that occurs there is viscous erosion.

(4) There is no chemical reactivity considered, and the particles do not rotate or interact chemically with the gas or one other.

(5) Since the particle sizes studied are substantially smaller than the local mean-free path of the gas, findings may be compared with free molecular theory in the validation case.

(6) In this study we do not take into account the effects of Saffman, Magnus, thermophoretic, or van der Waals forces. Thus, the only forces considered to act on a grain particle are particle-particle forces, particle-wall collision forces, drag (due to fluid-particle interaction), and gravitational force. It is expected that the other forces are negligible compared to these, especially because of the free molecular flow conditions existing in this work.

J. Solution methodology

A Lagrangian-Lagrangian multiphase model is developed in this study, wherein the solid lunar dust and lander gas exhaust have been considered as the Lagrangian phases. The gas phase is solved using the DSMC approach, while the DEM approach is employed for modeling the dust/granular phase. A gas-grain interaction model is used for considering momentum and energy exchange between the two phases. The lunar atmosphere is considered as vacuum. The specific convergence

criteria for each solver are provided in Sec. II A. The two phases evolve together in a transient simulation associated with lunar landing. It is computationally very challenging to run gas and grain phase simulations simultaneously due to huge differences in the relaxation time of each phase. Therefore, we have performed a two-way coupled simulation in a stagewise manner as follows: a steady-state gas flow field is first calculated using DSMC. It is demonstrated (refer to the Appendix) that steady state is indeed reached for DSMC simulations. Using the pure gas flow field, a granular flow field is determined using gas-grain interaction model (taking care of momentum and energy exchange between gas and grain phases) and DEM approach (taking care of grain-grain interactions).

As the coupled solver runs, particles begin to erode from the surface and move out of the vacuum boundary. The process continues until the number of eroded particles equals the number of particles exiting the domain, and the total kinetic energy associated with grains in the domain remains constant, as is shown concretely in the Appendix. At this point, we compute the average of the converged results and conclude this subcycle for the grain phase. During this subcycle, the grain phase reaches a steady state while passing through transients. The granular field data are used to modify the carrier gas field data using our gas-grain interaction model. During this process, the gas flow field jumps from one steady state to another after momentum and energy exchange with granular phase is considered. The modified gas flow field is again considered for updating the granular phase flow field. Thus, the iterative approach is followed two times, during which gas and grain phases transition from one state to another.

A more specific description of the different stages of dusty-gas flow simulation is given below for further clarity:

Stage 1: Simulation of gas flow through the nozzle is performed using an in-house DSMC solver, and nozzle exit properties are extracted.

Stage 2: Nozzle exit properties are used as input to the gas phase solver (NFS DSMC again, but slightly modified to work more efficiently for the free molecular regime), which will simulate plume impingement on the planetary body. Gas flow field is obtained for the entire domain and is used to evaluate the surface erosion rates or ejection of granular particles.

Stage 3: Keeping the gas-phase flow field unchanged, we now obtain grain phase results by running the gas-grain solver. Here grain-grain collisions are handled by DEM solver, while gas-grain interactions are modeled in the modified DSMC framework.

Stage 4: Gas-phase simulation using a gas-grain solver continues from the same time step where it ends in stage 2 to obtain updated gas-phase properties in the background of grain phase data.

Stage 5: The final results are obtained for the grain phase by rerunning the gas-grain solver in the gas background with updated gas-phase results from stage 4.

III. RESULTS AND DISCUSSION

We now present results for the cases described in Sec. II J. First, we explore the rocket plume flow fields obtained using the DSMC approach. A constant hovering height of 4 m is maintained throughout all simulations. Next, we examine lunar regolith flow as a basis for tracing particle trajectories utilizing DEM. A monodisperse system is employed for all simulations. The effects of particle size variation on the flow field are examined. We have selected a nominal particle size of 1 mm to demonstrate the impact of particles on the gas flow field and vice versa. Finally, we compare velocity and temperature to examine the impact of two-way coupling on the rocket plume and lunar particles.

A. Stage 1: Simulation of the nozzle flow field of lunar lander

This study examines a contoured nozzle, which was designed based on the geometry utilized in prior research by Hammock *et al.* [70] and Morris *et al.* [23]. A schematic of the nozzle is depicted

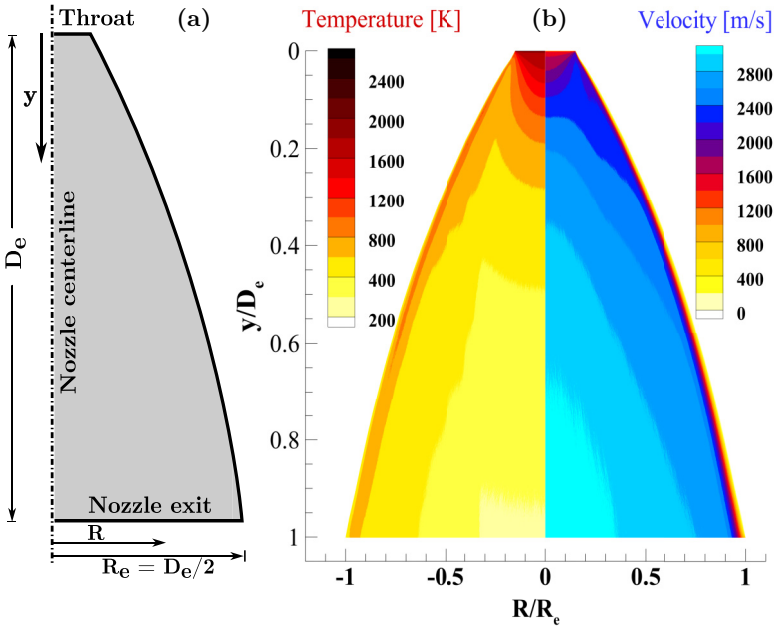

FIG. 7. (a) Schematic of a nozzle; (b) temperature and velocity contours of the flow field in the nozzle. D_e and R_e represent the diameter and radius of the nozzle exit, respectively.

in Fig. 7(a). We employ a two-dimensional DSMC solver for the steady gas flow expansion via the nozzle into the lunar atmosphere, which is at near-vacuum state. The diameters of the nozzle exit and throat are, respectively, $D_e = 1.62$ m and $D_t = 0.26$ m. At the nozzle throat, the pressure, velocity, and temperature of the flow are 1.44 bar, 1214 m/s, and 2458 K, respectively. Water vapor is considered as the rocket exhaust.

Figure 7(b) presents spatial fields of velocity and temperature. The contours presented in Fig. 7(b) illustrate the internal flow properties through the length of the nozzle, used during the *Apollo* mission. The normalization of flow properties is carried out with their corresponding throat values, whereas the normalization of the horizontal (or radial) distance, R, is performed using the nozzle exit radius, R_e. The nozzle geometry causes the gas to expand at the throat, and a compression wave begins at the nozzle throat and propagates towards the exit, causing an abrupt shift in the internal gas flow properties, including velocity, temperature, pressure, and density. Temperature decreases and velocity increases towards the exit. Figure 7(b) further demonstrates the presence of a low-speed boundary layer. The flow properties are extracted at the nozzle exit, which will be taken as inlet conditions for Stage 2, involving the impingement of a vertical plume on the lunar surface. At the nozzle outlet, the variation of velocity, density, and temperature with $\overline{R} = R/R_e$ is displayed in Fig. 8, where R is the distance measured from the nozzle centerline. For symmetrical reasons, we focus on the right half of the region. Note that the quantities presented in Fig. 8 are scaled by normalizing their respective values at the throat. Figure 8(a) shows the normalized velocities at the nozzle exit in the horizontal $\overline{V}_h = V_h/V_t$ and vertical $\overline{V}_v = V_v/V_t$ directions. Here V_h and V_v are the horizontal and vertical velocities at the exit, with V_t being the velocity at the throat. It may be inferred that the nozzle is well designed as the vertical velocity $\overline{V}_v$ remains almost constant away from the viscous boundary layer. The thickness of the viscous boundary layer is comparatively small, and its impact on the engine's output is negligible. On the other hand, the horizontal velocity is the lowest at the centerline and subsequently increases monotonically in the one-third region. After a sudden drop at about 0.4 m, it further rises largely monotonically. In Fig. 8(b), at the outset, we note the similarity in the variation of the scaled density $\overline{\rho} = \rho/\rho_t$ and temperature $\overline{T} = T/T_t$,

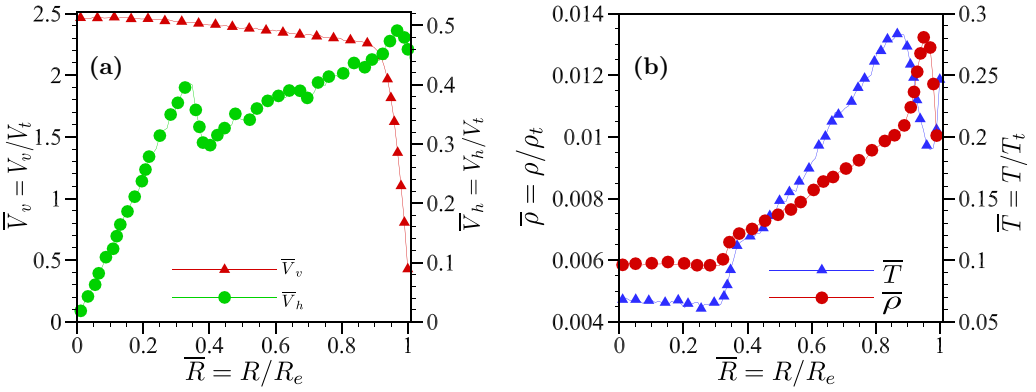

FIG. 8. Variation of flow properties at the nozzle exit. (a) Normalized vertical and horizontal velocities, and (b) normalized density and temperature.

where ρ and T are density and temperature at the exit, respectively, with ρ_t and T_t being their counterparts at the throat. Contrary to velocity, they vary less significantly as one moves away from the center. There is a steep rise in both $\overline{\rho}$ and $\overline{T}$ between $\overline{R} \approx 0.3$ and 0.4, correlating well with a corresponding fall in the horizontal velocity. The abrupt alterations in properties can be attributed to the presence of shock inside the nozzle. Beyond $\overline{R} = 0.4$, $\overline{\rho}$ and $\overline{T}$ exhibit a nonmonotonic variation and rapidly decrease as the gas expands into the near-vacuum conditions of the moon. Near the nozzle centerline ($\overline{R} \approx 0$), $\overline{\rho}$, $\overline{T}$, and $\overline{V}_h$ have minimum values, while $\overline{V}_v$ has the maximum. It is worth remarking that the variation of velocity, density, and temperature are in fair qualitative agreement with those reported during the *Apollo* mission [23]. Finally, we compute the average values of density, temperature, and velocity at the exit, which are 1.03×10^{-3} kg/m^3, 553 K, and 2779 m/s, respectively, which will be utilized as input to the next stage.

B. Stage 2: Expansion and impingement of rocket plume on the lunar atmosphere and surface

Here we examine the pure plume flow (no dust) into the lunar environment and its impingement on the lunar surface, which is assumed to be flat. As stated earlier, the average flow properties at the nozzle outlet are employed as input. The lander height and engine specifications determine plume structure and, in turn, erosion dynamics. The vertical velocity and translational temperature fields are displayed in Fig. 9. Here the average kinetic energy associated with the translational motion of gas particles is referred to as the translational temperature. On the other hand, the overall temperature represents the sum of the average kinetic energies corresponding to translational, rotational and vibrational motion of gas particles. In this near-vacuum environment, the gas expands rapidly, creating a shock wave. It is evident in Fig. 9 that the streamlines are almost straight near the plume axis, leading to a normal shock near the axis where the flow impinges on a flat surface. These findings are consistent with previous reports [21,32]. When we move away horizontally from the center of the nozzle, the streamlines become oblique, and the lunar surface serves as a ramp for the incoming flow, leading to a series of oblique shocks. A recognizable bow shock formation occurs starting at the depth of 2.7 m from the nozzle exit. The maximum intensity of this shock is located at the center of the nozzle, and its magnitude diminishes as it propagates outward. The investigation of plume behavior involves an examination of both vertical and horizontal velocities, as well as the average kinetic energy associated with translational motion. While Fig. 9 provides insight into the translational temperature and vertical velocity variables, it is necessary to further analyze the total kinetic energy of the gas and the velocity at which the plume expands horizontally to far-field locations. The horizontal velocity and overall temperature contour of the plume for the entire domain of interest are illustrated in Fig. 10. Here the point of impact underneath the shock

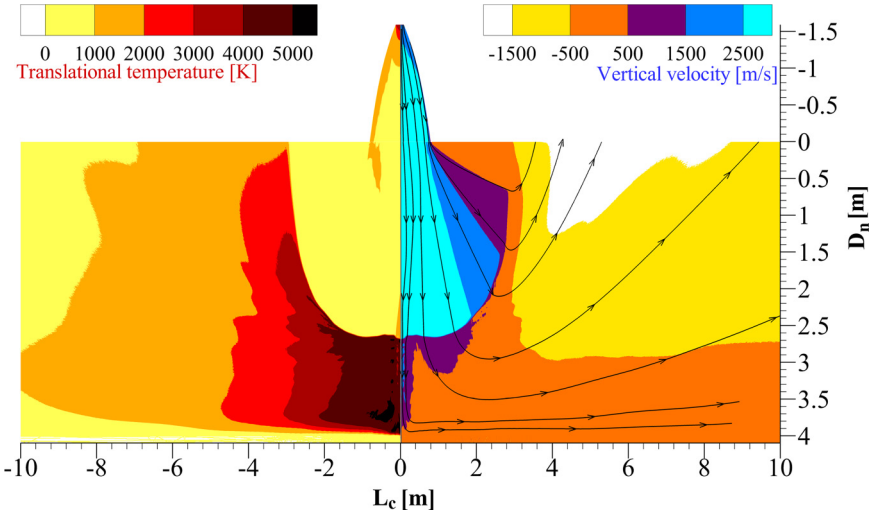

FIG. 9. Spatial distribution of temperature and vertical velocity with streamlines. D_n represents the vertical distance from the nozzle exit, and L_c denotes the distance from the nozzle centerline.

generates a positive pressure gradient in the radial direction, which causes a high-velocity flow in the outward direction. The interaction of plume gas molecules with the lunar surface stimulates an upward flow of the plume gas. Following the impact, there is a further expansion of the flow as a consequence of the vacuum boundary condition applied in the simulation. This leads to an increase in flow velocity and a reduction in temperature. Let us now examine the density field in Fig. 11.

Note that the density is maximum around the impingement area and the decrease in magnitude occurs swiftly and diminishes to extremely small levels along both the vertical and radial directions within the lunar environment. The transition from a continuous to a rarefied flow field is evidenced by a significant variation in the density contour. When considering the particle transport in a rarefied environment, the density of the rocket plume is crucial since it influences the drag. We compute that the greatest far-field mean-free path is 0.02 m, with a Knudsen number of 2×10^4 based on the particle diameter. This shows that the local flow is in the free molecular regime, which suggests

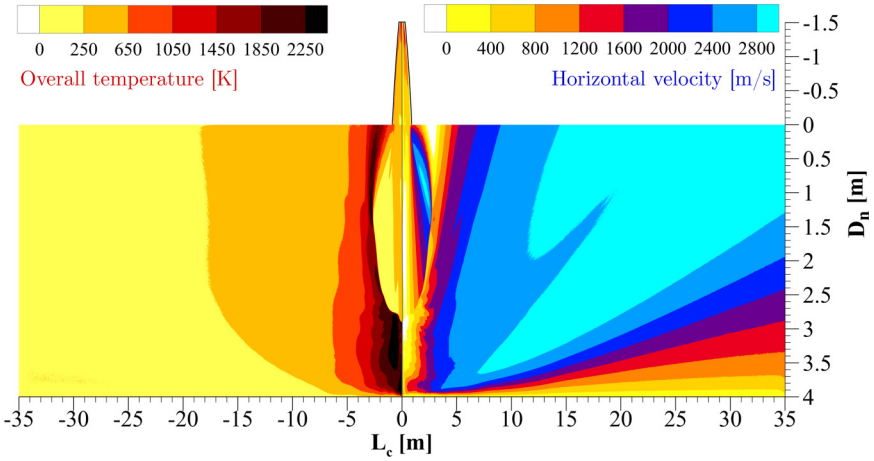

FIG. 10. Spatial distribution of the horizontal velocity and overall temperature for the entire domain.

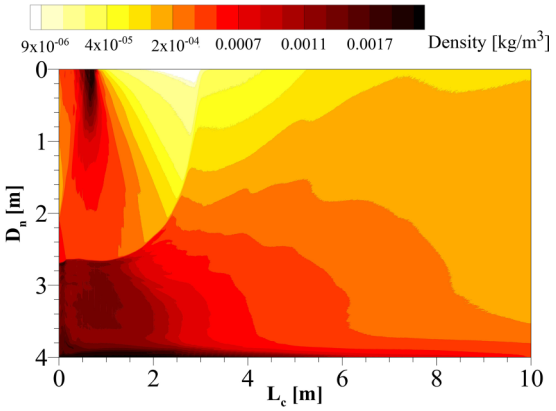

FIG. 11. Contours representing the density flow field variation.

against the use of a continuum approach to compute drag for particles. Accordingly, we carry out free molecular flow simulations, by simulating free molecular flow of gas over an isolated granular particle to determine the amount of momentum and heat transfer between the gas and a particle. In order to represent particle drag and heat flux, the information given in Sec. II C is utilized to compile a look-up table, which consists of the normalized heat flux and coefficient of drag variations with speed ratio, as shown in Fig. 3. To assess the statistical error linked to our model, we performed a statistical analysis for our DSMC results on the particle velocities within a cell across various time steps. This investigation is replicated for multiple cells within the domain. Utilizing the data set, we computed the standard error, which came out to be approximately 4% of the mean value for DSMC simulations. Due to the minute size of the error values, they are not visually depicted in the graphical representations. Consequently, error bars have not been incorporated into the plots.

C. Stage 3: Simulation of the motion of lunar particle

Maintaining the same gas-phase flow field, grain phase results have been acquired by running the gas-grain solver. Here grain-grain and grain-wall collisions are handled by the DEM solver, while gas-grain interactions are modeled in the modified DSMC framework. We employed a comparable approach to compute the statistical error in DEM simulation, as employed for DSMC simulations. It is observed that standard error is below 1% of the mean value.

1. Erosion of lunar particles

When a rocket plume hits the ground, it applies normal and tangential loads that may cause erosion of the soil. The model stated in Sec. II E suggests that the plume impingement on the lunar surface causes viscous erosion, facilitated by the shear stress applied on soil due to the motion of gas over the lunar surface [71]. Equation (26) establishes a direct proportionality between the erosion flux and the shear stress. This model also treats dynamic pressure as applied shear stress [21], which establishes the proportionality of dynamic pressure and erosion flux. The spatial distribution of dynamic pressure is presented in Fig. 12. At first sight, we observe that the dynamic pressure decreases as we move away from the nozzle centerline. For clarity, Inset 1 in Fig. 12 shows its variation with distance from nozzle centerline at 3.5 m depth below the nozzle exit. As per the observation made in Inset 2 of Fig. 12, it can be inferred that the erosion flux begins to increase at around 0.6 m from the nozzle centerline, peaking approximately at a distance of 5 m, and tends to vanish beyond 7 m from the nozzle centerline. This phenomenon is attributed to the existence of a normal shock, which generates straight streamlines, as shown in Fig. 9, and this leads to minimal viscous erosion within that region. As the streamlines gradually incline downward, the

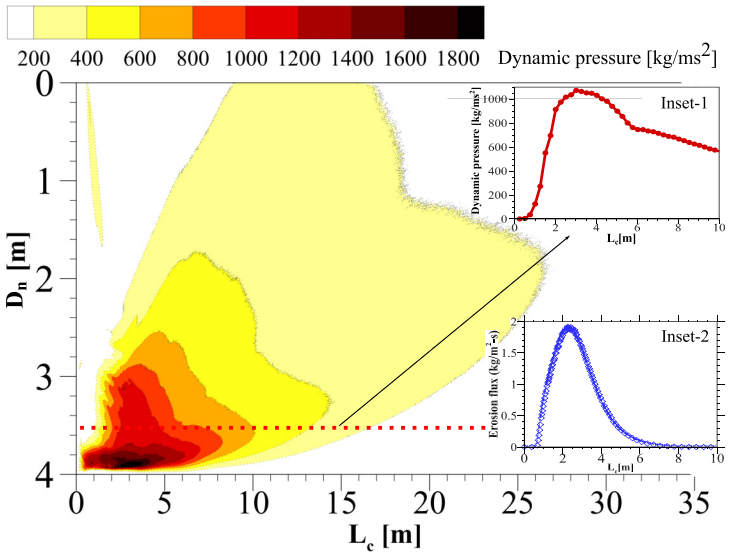

FIG. 12. Contours representing the dynamic pressure responsible for erosion. Inset 1: Dynamic pressure variation at the depth of 3.5 m below nozzle exit. Inset 2: Erosion flux variation at the lunar surface.

level of viscous erosion and erosion flux correspondingly rises. A qualitative proportionality may be observed through a comparison between Inset 1 and Inset 2 of Fig. 12. The change in erosion flux is thought to be caused by a shift in the dynamic pressure that occurs in the radial direction outward from the nozzle's central axis. Because the dynamic pressure is directly proportional to the density and square of the velocity, as given in Eq. (28). Once the rate of decrease in density exceeds the rate of increase in velocity, the dynamic pressure in the far field experiences a significant reduction. Similarly, as a result of the relatively low horizontal velocity close to the nozzle centerline, the dynamic pressure is also low in the vicinity of the plume axis. Based on the erosion rate, granular particles are introduced into the domain at zero speed and a temperature of 200 K [24].

2. Trajectory of eroded lunar particles

Figure 13 shows the trajectory followed by lunar particles after erosion. The visuals depict various instances of a particle simulation, illustrating the progression of particles over both spatial and temporal dimensions. At the outset, particles undergo erosion until the erosion radius. The distance at which erosion ceases is commonly referred to as the erosion radius. Particles exchange momentum and energy with the plume, thereby getting advected/entrained in the same direction as the plume's movement. We find that Stokes number is 0.002 near the surface when the characteristic length is the plume impingement height ($H = 4$ m), while it is roughly 0.005 for the far-field distance taken as a characteristic length. Therefore, it can be inferred that the predominant mechanism of the flow is advection, and the movement of particles observed in Fig. 13 confirms the streamlines illustrated in Fig. 9. This is supported by Fig. 14(a), which illustrates that the ratio of vertical to horizontal velocity is low, indicating that the vertical velocity is negligible compared to the horizontal velocity. As depicted in Fig. 14(b), this results in a very low angle of movement for particles close to the lunar surface. As the simulation progresses, particles scatter throughout the domain. The model stated in Sec. II C suggests that the flow that surrounds dust particles is in a state of free molecular motion. The validity of this presumption has been verified by ascertaining that the mean-free path is significantly greater than the largest diameter lunar particle simulated. In the initial phases, the forces originating solely from the gas flow exert a dominant influence,

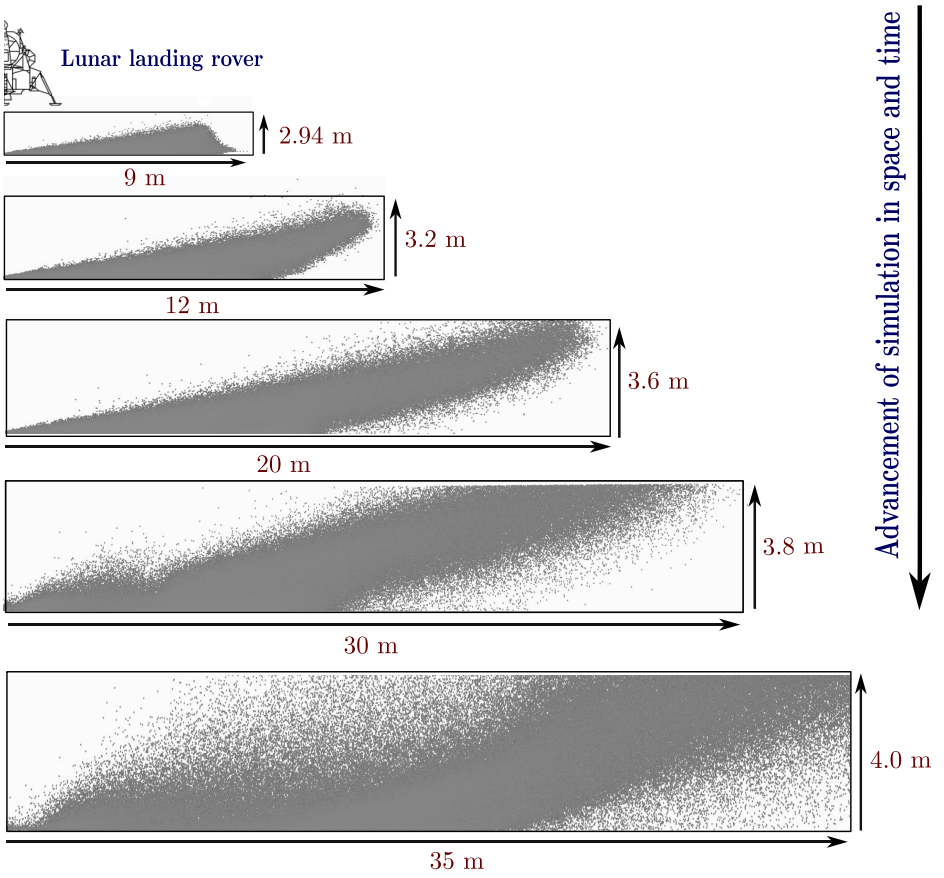

FIG. 13. Trajectories of lunar particles at different time instants.

promptly establishing particle velocities in direct correlation with the gas velocity field. It is only in the distant regions, as the gas density field diminishes, that we anticipate particle collisions, inertia, and the gravitational force to assume a more predominant role. Due to the momentum exchange

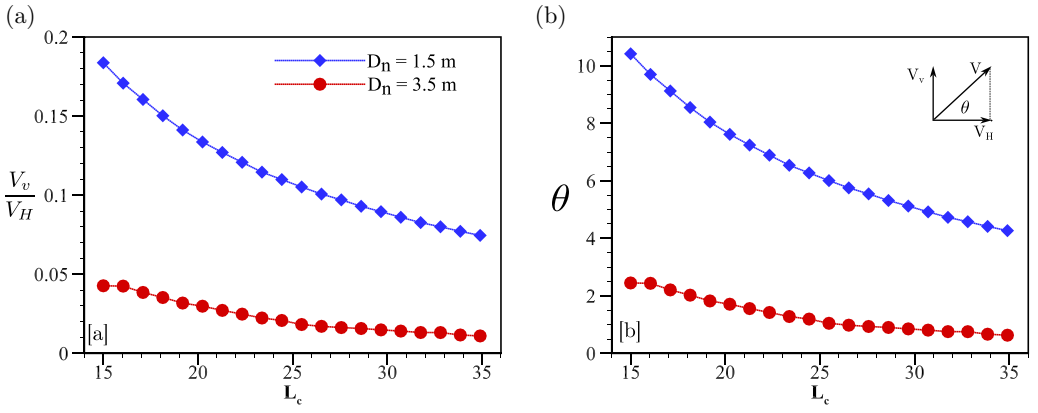

FIG. 14. Variation of (a) the vertical(V_v) to horizontal(V_H) velocity ratio and (b) inverse tangential of V_v/V_H in degrees, at two depths from the nozzle exit.

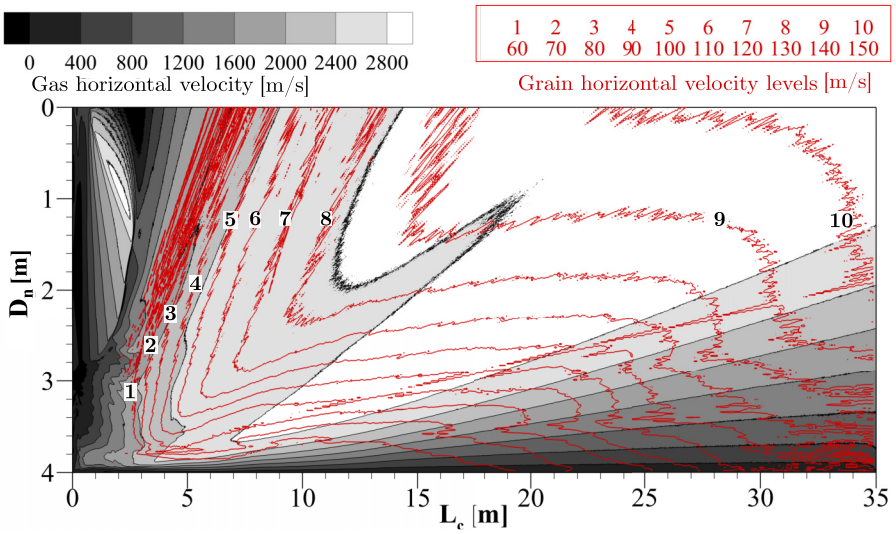

FIG. 15. Horizontal velocity contours of the gas and grain phase.

with the gas phase, the granular particles get entrained with the gas flow. Particles with low inertia quickly adapt to the flow speed and direction. These speeding particles are hardly impacted by the flow downstream since the gas quickly achieves low density values (see Fig. 11). The high-velocity plume flow is less likely to carry large particles than it is to carry smaller particles because of inertia and gravity. As a result, the larger diameter lunar particles will gain less velocity and the height gained by them is also less consequences. Additionally, particles that are situated farther from the centerline encounter gas flow with a lower density, and as a result, experience less drag force. Figure 15 displays the horizontal velocity flow field of the plume superimposed over the horizontal velocity zones of the granular phase for $d = 1$ mm, and thus explains the influence of background gas on particles. Such an observation correlates with a noticeable decline in density beyond a certain distance, displayed in Fig. 11. Consequently, we note an increase in the velocity of lunar particles in Fig. 15 as we move in downstream direction from the nozzle centerline, which explains the influence of background gas on particles. Trajectories of ejecta depend upon various factors, including particle size, the radial location of a particle on the surface before erosion, and collisional dissipation. Next, we examine how the trajectory evolves in the absence or presence of interparticle collisions.

3. Influence of interparticle collisions

Figure 16 displays the horizontal velocity contours of lunar particles in the absence and presence of interparticle collisions. Clearly, we notice that interparticle collisions play a significant role in particle movement. Figure 16(a) illustrates both the entrainment of particles by the gas as well as the subsequent advection of those particles. Particles attain a maximum height of 2 m, without interacting with each other. When interparticle collisions are enabled, particles achieve a vertical displacement of over 4 m and disperse throughout the domain.

4. Effect of collisional dissipation

Here we consider smooth particles with unity restitution coefficient, implying no dissipation during collisions. Other parameters remain unchanged as shown in Table II. Data are extracted along vertical lines at two locations from the nozzle centerline (15 m and 35 m) and two horizontal lines at a depth of 1.5 m and 3.5 m from the nozzle exit. A comparison is shown between the data for nondissipative and dissipative grains in Fig. 17. As expected, Figs. 17(a) and 17(b) demonstrate

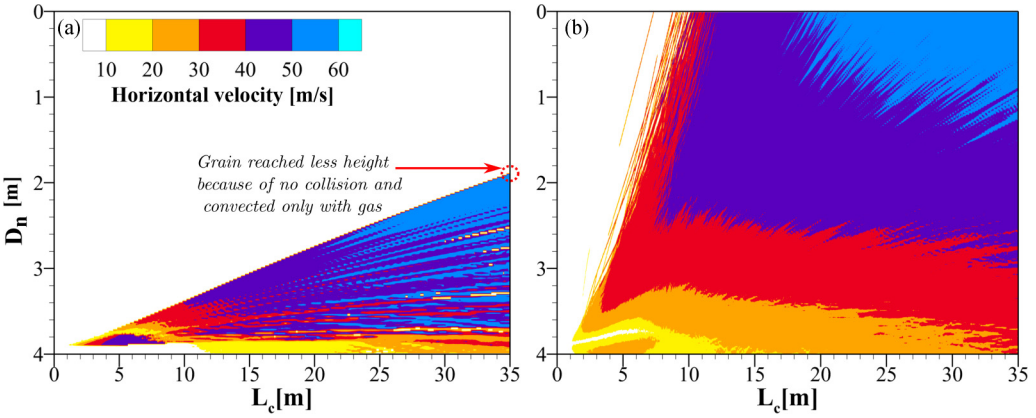

FIG. 16. Horizontal velocity contours of lunar particles in the (a) absence and (b) presence of interparticle collisions.

that nondissipative particles have higher velocities as compared to their dissipative counterparts. The difference in velocity is attributed to the dissipation of energy. This observation indicates that an increase in collisions between lunar particles results in a corresponding growth in the amount of energy dissipated.

5. The effect of particle diameter on dust spray

The influence of particle size has been analyzed keeping the gas flow-field unchanged, i.e., constant dynamic pressure. Here we have varied the diameter of particles between 0.1 and 5 mm, covering mostly the size distribution of lunar soil defined by Carrier *et al.* [69]. We note an increase in the number of ejected particles as the particle diameter reduces. Table III shows the number of particles ejected as particle diameter reduces. The starting radial location and particle size significantly impact the trajectories of ejecta.

Figures 18 and 19 present the spatial distribution of horizontal velocity and temperature for particles of size 1 mm and 100 μm, respectively. It is important to note that the velocity is determined by averaging the velocities of all dust grains contained within a specific computational cell. Particles with a diameter of 100 μm exhibit a maximum velocity that is approximately four times greater than those with a size of 1 mm. Similarly, the maximum temperature for by 100 μm is also higher than

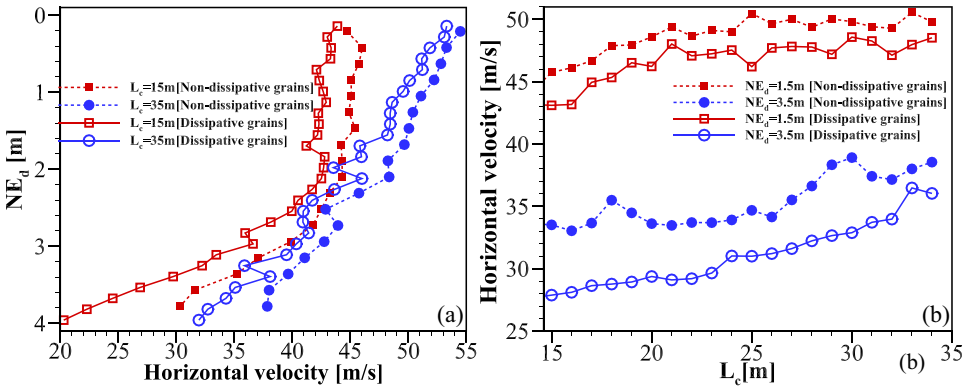

FIG. 17. Horizontal velocity comparison between nondissipative and dissipative grains at (a) two horizontal locations from the nozzle centerline and (b) two depths from the nozzle exit.

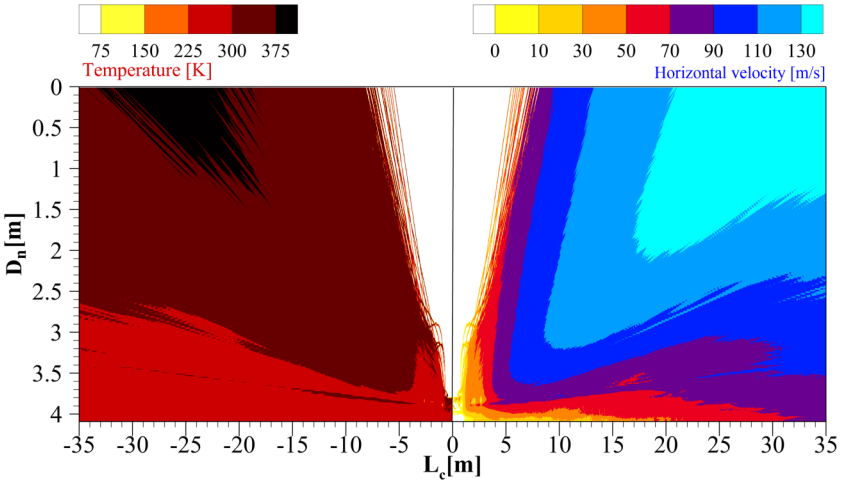

FIG. 18. Spatial distribution of horizontal velocity and temperature for 1 mm diameter particles.

1 mm particles. The high-velocity plume is less likely to carry big particles than small ones because with the same amount of momentum exchange the small particles will get larger velocity, and the number of smaller particles ejected is large for the same plume flow field. Weight dominates drag, when particle size grows, leading to parabolic trajectories within the numerical domain. Let us now look at the momentum of 1 mm and 100 μm particles with the largest horizontal velocity of 130 m/s and 450 m/s as shown in Figs. 18 and 19. The momentum of 1 mm diameter lunar particle comes out to be 1.83×10^{-4} Ns, which is larger than the momentum 8.47×10^{-7} Ns of a 100 μm particle. The difference is of several orders of magnitude. Therefore, we can conclude that the bigger particles have more damage potential than the smaller ones. In spite of the fact that particle velocity reduces with increasing particle size, both momentum and kinetic energy grow with increasing particle size. The inverse relationship of velocity with particle size may be understood in terms of the particle relaxation time for Stokes flow at very low pressure, which states that the particle relaxation time is given as $\tau = m_p C_c/3\pi\mu D_p$, where m_p is the particle mass, μ is the dynamic

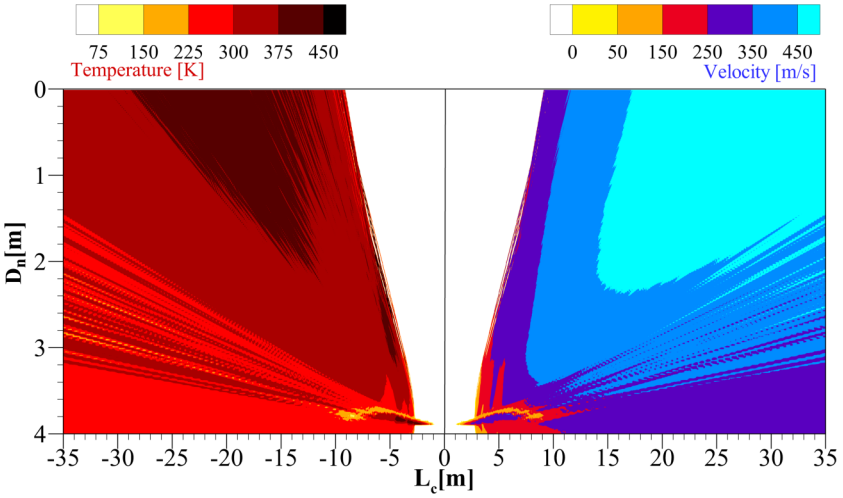

FIG. 19. Spatial distribution of horizontal velocity and temperature for 100 μm diameter particles.

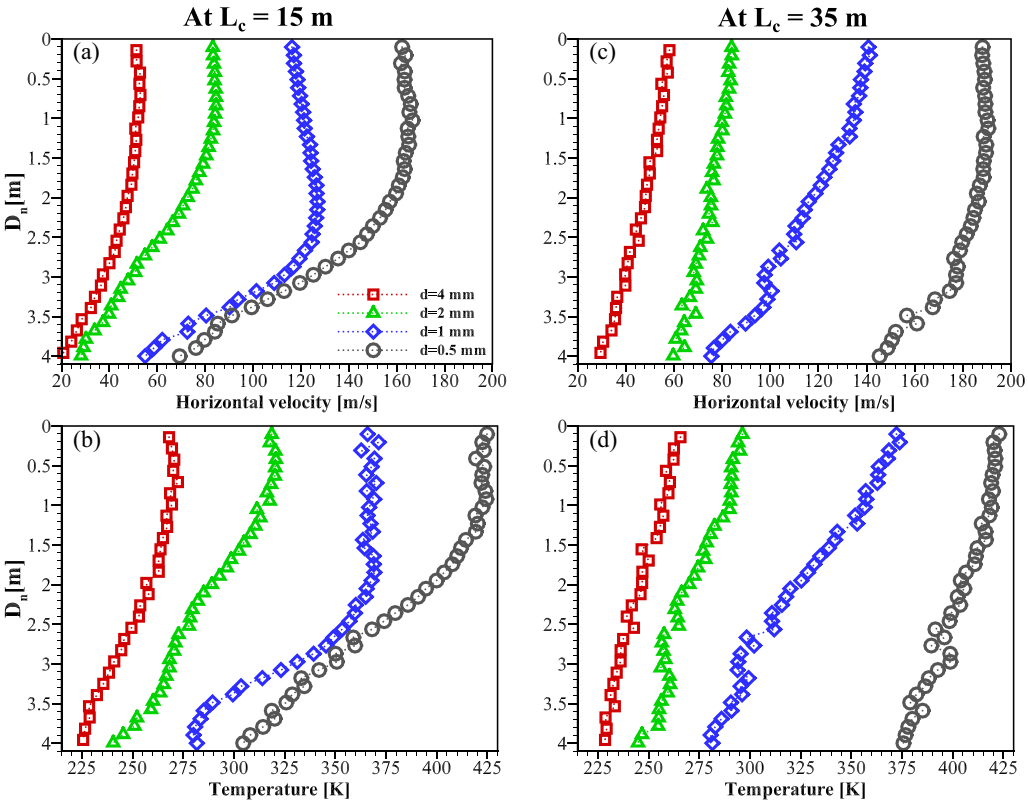

FIG. 20. Horizontal velocity and temperature variations at different far-field locations from the nozzle centerline. Legend for all plots are given in (a).

viscosity, D_p is the particle diameter, and C_c is the slip correction factor. In the free molecular regime, $\mu \propto \rho_g \lambda \sqrt{T}$ and $C_c \sim K_n = \lambda/D_p$, the relaxation time, $\tau \propto \rho_p D_p/\rho_g \sqrt{T}$. For a given particle density (ρ_p) and diameter (D_p), the relaxation time τ is given as $\tau \propto 1/\rho_g \sqrt{T}$. Hence, as the flow extends throughout the lunar surface, the resulting increase in relaxation time is expected. Since the relaxation or reaction time is directly proportional to the particle diameter, as mentioned above, the relaxation time increases as particle size increases. For larger particles, the relaxation period is quite significant, leading to lower peak velocity and temperature. Likewise, an increase in particle size results in greater radial displacement for larger particles, while causing smaller particles to uplift at a faster rate. We now present in Fig. 20 the variation of far-field horizontal velocity and temperature for several particle diameters at two locations, 15 m and 35 m from the nozzle centerline, with the depth from the nozzle exit. We note in Fig. 20 for a fixed particle size that the velocity and temperature decline as one descends from the nozzle exit plane towards the lunar surface, and at a given depth, the velocity and temperature reduce with increasing particle size. We observe the same in Fig. 21, which shows the variation of far-field horizontal velocity and temperature with distance from the nozzle centerline for several particle diameters at two depths 1.5 m and 3.5 m from the nozzle exit. It is clear from Figs. 20 and 21 that the difference in velocity and temperature increases as the particle size decreases. These variations in particle velocity lead to size-based separation as the particles travel into the far field. Here smaller particles exhibit a faster thermal response, reaching temperatures close to 425 K, while larger particles attain a maximum temperature of approximately 250 K. The heated grains dissipate energy as they expand outward.

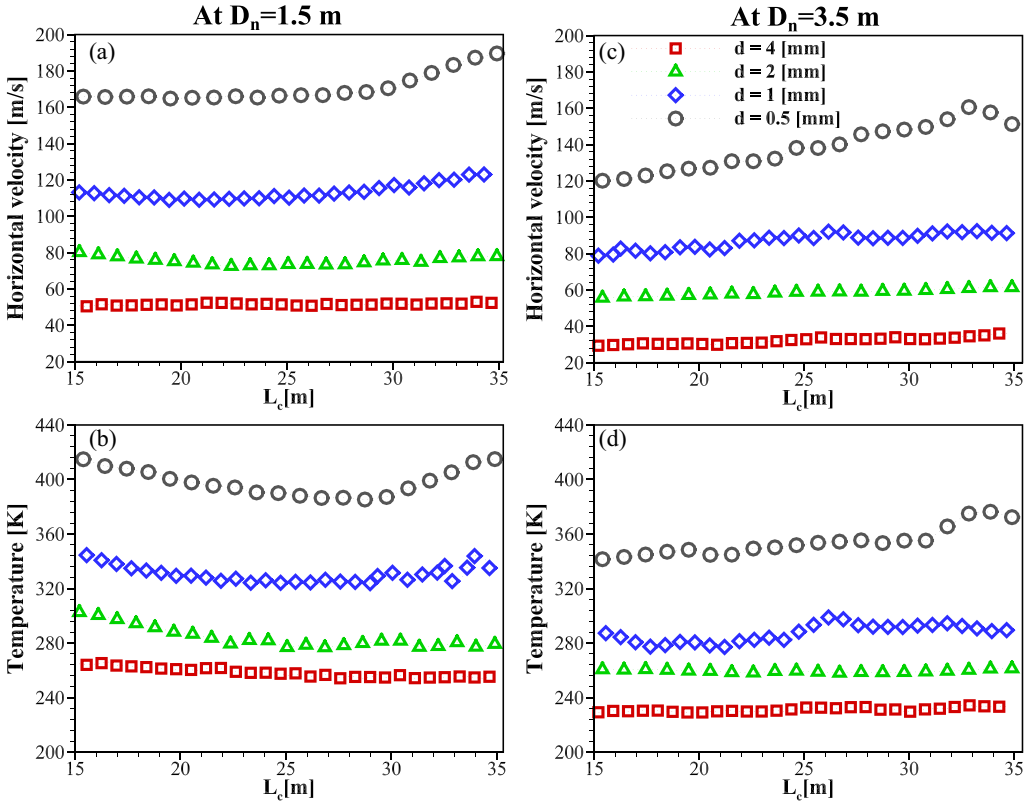

FIG. 21. Horizontal velocity and temperature for two depths from the nozzle exit. Legend for all plots is given in (c).

Other dust sizes follow similar trends. Our particle velocity estimation will serve as a valuable tool for forecasting the potential harm caused by lunar regolith ejecta when a space vehicle descends.

D. Stage 4: Effect of lunar particles on plume flow field

We now examine the effect of lunar particles on the plume flow field. The lunar particles, which are initially stationary, eject out from the surface, after which they get entrained with the plume flow, and then gain momentum from the plume flow field. Concurrently, the flow field of the plume undergoes a reduction in momentum of equal magnitude. Furthermore, the plume also imparts energy to the lunar particles via thermal means/heat transfer. The introduction of particles has been observed to impede the expansion of gas by transferring some momentum and energy to the granular phase. This phenomenon is reflected in changes to the velocity and temperature of the plume flow field. Variations of the horizontal velocity and temperature for three far-field locations from the nozzle centerline are shown in Figs. 22(a) and 22(b), respectively. Two locations, 1.5 m and 3.5 m, down from the nozzle exit have been chosen to extract the data and used to compare properties, as shown in Figs. 23(a) and 23(b). When comparing one-way and two-way coupled models, it has been observed from Figs. 22 and 23 that the two-way coupled model results in lower plume horizontal velocities and overall temperatures.

The slowing of gas near the surface results in a loss of dynamic pressure and in turn an overall decreased erosion rate. A more detailed impact of the two-way coupled model on gas flow field and thereby the erosion rate can be observed from Fig. 24. It can be noted that the erosion profile changes

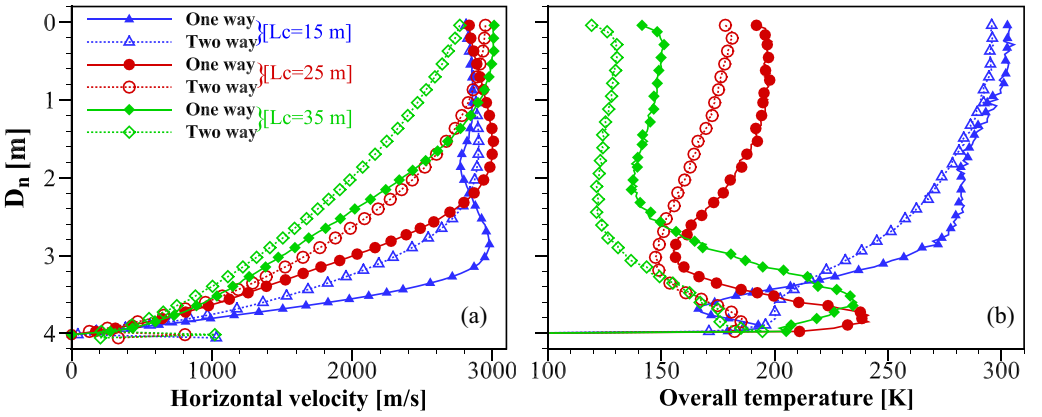

FIG. 22. Comparison of (a) horizontal velocity and (b) temperature, between one-way and two-way coupled models for various far-field distances from the nozzle centerline.

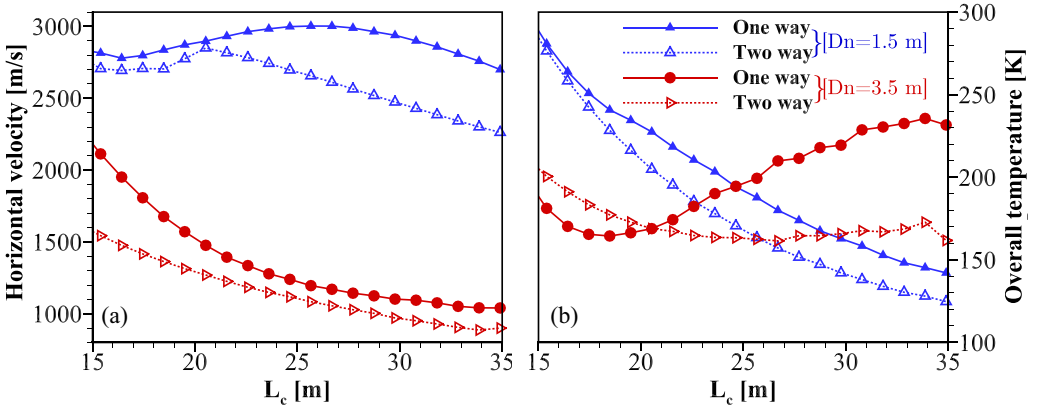

FIG. 23. Comparison of (a) horizontal velocity and (b) temperature, between one-way and two-way coupled models for various depths below the nozzle exit.

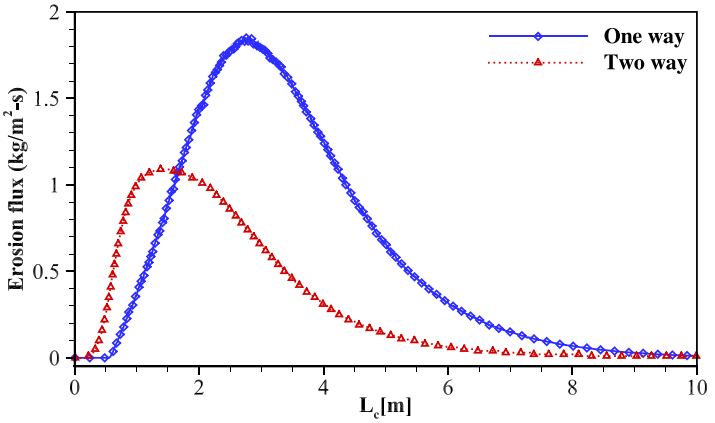

FIG. 24. Comparison of erosion profiles between one-way and two-way coupled models.

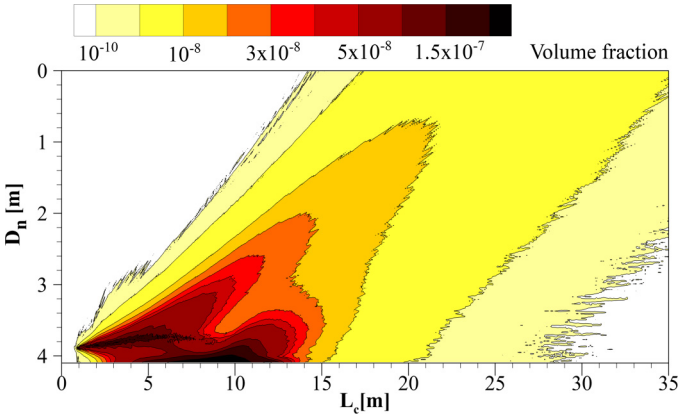

FIG. 25. Contour showing volume fraction variation across the whole simulation domain for 1 mm diameter lunar particles.

significantly following the introduction of particles into the domain. These changes stem from variations in both density and velocity of the gas, caused by the momentum and energy exchange with grain phase. Consequently, the erosion profile undergoes a noticeable change, including shift in the peak of erosion. The erosion profile for two-way coupled framework can also be found to get narrowed, as momentum is sapped from the gas when dust becomes entrained, resulting in reduced dust emission downstream. The difference in the peak horizontal velocity and temperature between one-way and two-way coupled models increases, as we move away from the nozzle centerline, as shown in Figs. 22(a) and 22(b), respectively. Gas loses momentum and energy as it expands in the presence of particles. It is observed from Figs. 23(a) and 23(b) that at 1.5 m depth from the nozzle exit, the difference in horizontal velocity and temperature increases as we move away from the nozzle centerline. But at a depth of 3.5 m from the nozzle exit, Fig. 23(a) shows that the difference in horizontal velocity decreases because of the presence of more particles at 15 m than 35 m distance from the nozzle centerline. To clarify and explain this, the distribution of particles is depicted in Fig. 25 in terms of volume fraction, which is defined as the ratio of the volume occupied by solid particles to the total volume of the region. In the whole domain, the volume fraction remains very low. At the surface, where erosion occurs, the volume fraction is substantially greater. As we move away from the surface and along the horizontal distance, its intensity decreases swiftly. The momentum exchange increases for a higher particle concentration. thereby reducing the gas velocity correspondingly.

E. Stage 5: Effect of two-way coupling on particles

Here we examine the effect of two-way coupling on granular flow fields. For analyzing further, we have extracted the data at 15 m distance from the nozzle centerline and at 1.5 m depth from the nozzle exit plane for 1 mm and 5 mm particles. The horizontal velocity and temperature of lunar particles for both one-way and two-way coupled models are compared in Fig. 26.

We note that for the two-way coupled model, the granular speed and temperature are lower compared to the one-way coupled model. The maximum radial velocity of the 5 mm particles is reduced from 66 m/s (for one-way coupled model, i.e., when the gas field is uncoupled) to 59 m/s when gas and grain phases are two-way coupled. Likewise, the maximum radial velocity of the 1 mm particles is reduced from 125 m/s to 105 m/s. The difference arises because of the reduction in the momentum and energy of two-way coupled gas, which in turn affects the particle motion. At a distance of 15 m from the nozzle centerline, the difference in velocity and temperature between the one-way and two-way coupled model is smaller for 5 mm particles in comparison to 1 mm particles, as shown in Figs. 26(a) and 26(b). The results also indicate that there is a significant

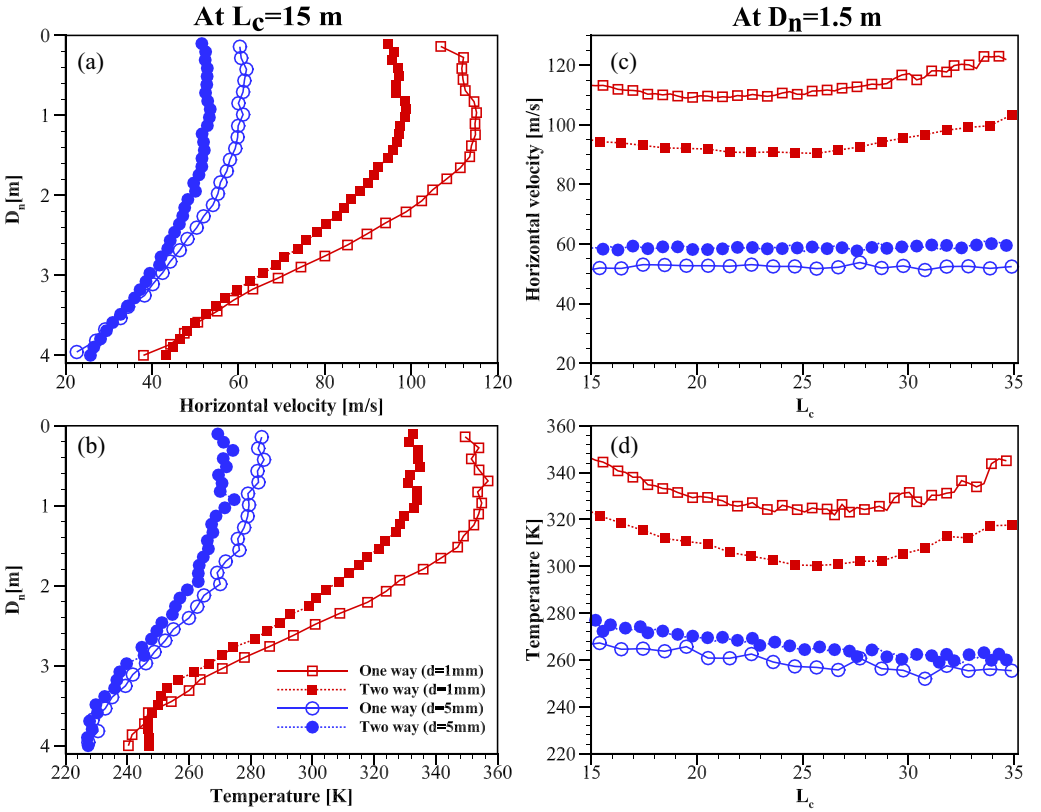

FIG. 26. Comparison of (a), (c) horizontal velocity and (b), (d) temperature, between one-way and two-way coupled models for 15 m far-field distance from nozzle centerline and 1.5 m depth below the nozzle exit.

difference in horizontal velocity and temperature near the nozzle exit, as opposed to the lunar surface. Similarly, Figs. 26(b) and 26(d) depict that at a depth of 1.5 m from the nozzle exit, the difference in temperature is less for 5 mm particles than 1 mm particles. Even at a very low volume fraction, as shown in Fig 25, the momentum and energy exchange between the two phases remains considerable. This is due to the high speed of the gas phase (∼km/s), such that the momentum and energy exchange between the two phases are still significant.

IV. CONCLUSIONS

While approaching an intended lunar landing location, a variable-thrust engine plume can cause significant surface erosion and dust dispersion. A certain amount of useful quantitative or qualitative information could be extracted from videos and photographs from previous missions; however, they do not provide enough data to understand the multiphysics phenomena associated with dust dispersion due to plume impingement, which may be necessary for successful future missions. Therefore, development of a computational framework that can model and explain such phenomena and the details of dust dispersion with particle volume fraction, velocity, and angular distribution of ejected grains along with their temperature is necessary for a given landing scenario. To this end, a two-way coupled Lagrangian-Lagrangian framework was developed in this work by coupling DSMC and DEM approaches, through a gas-grain interaction model, which was validated by comparing the results obtained with theory. The DSMC-DEM coupled framework was used to create a full-scale model of lunar dust transport in response to rocket plume impingement.

The total mass erosion rate was obtained by invoking a regolith erosion model, which was fine-tuned to match data with the *Apollo* data at different hovering altitudes [32]. An in-house DSMC-based flow solver was used to compute the plume flow field, which includes the nozzle's internal compressible flow and the near-field plume gas flow that suddenly expanded into vacuum. On the other hand, the DEM method was used to determine the grain-grain interactions and granular flow field. The gas phase was coupled to the grain phase through momentum and energy exchange by an in-house interphase coupling model. Thus, using the present two-way coupled DSMC-DEM solver, with our gas-grain interaction model for momentum and energy exchange, we can predict not only the velocities/kinetic energies of gas and grain phases, but also their temperature field. Such a solver is not yet available to the best of our knowledge. This kind of information (velocity and temperature for grains phase) can be important for the consideration of spacecraft designers from the standpoint of safety of sensitive electronic surfaces, solar panels, or even the viewpoint of surrounding hardware. To make the whole framework computationally tractable, drag and heat transfer coefficients were precalculated for a range of flow situations by performing three-dimensional DSMC simulations of gas flow over a single spherical granular particle using an in-house flow solver. In the simulations of dusty gas flows, the same data were used in the form of a look-up table. The solver is used in a stagewise manner till steady state is reached by each solver.

Some of the key findings of our numerical investigation of lunar dust dispersion upon plume impingement using an in-house DSMC-DEM solver are summarized here:

(1) The simulations yielded a particle velocity range spanning from 50 m/s to 450 m/s, corresponding to particle sizes ranging from 5 mm to 100 μm, respectively, observed at a distance of 15 m from the nozzle centerline. The corresponding range of angles for particle trajectories was found to vary from 2° to 15° for all particle sizes. The determination of the range of angles at which particles move is valuable for the design and development of mitigation techniques. The size and associated velocities of these particles play a crucial role in defining the momentum transferred to the surrounding structures, thereby influencing the choice of landing location for effective impact mitigation.

(2) There has not been any dedicated research in the literature exploring the impact of particle diameter on two-phase flow dynamics. The present study compares the dust-dispersion for particles having different diameters. It was found that the size of the grain particle had a significant impact on both the trajectory it takes and its properties. An increase in the size of a grain particle was found to cause a reduction in both the peak grain velocity and temperature.

(3) Studies so far had primarily focused on using low-diameter grain particles with velocities falling in the range of ∼km/s. However, as we delved into the realm of larger diameter particles, as studied in this work, we observed significantly higher momentum transfer and increased potential for high-impact collisions and damage.

The particle velocity was found to be primarily influenced by the gas velocity field in the near-field region, as the forces exerted by the gas flow significantly outweigh other forces. It is only in the far-field regions, where the gas density diminishes, that we expect particle collisions, inertia, and gravity to become predominant factors.

(4) As one moves away from the plume axis along the lunar surface, particle relaxation is seen to be delayed owing to the rapidly expanding flow in the radially outward direction. However, in the context of aerodynamic simulations conducted thus far, particle trajectories have primarily been determined by the streamlines of the gas flow.

(5) Effect of grain properties on gas flow field was analyzed, as well as the effect of gas flow field on grains. It is observed that gas flow field loses momentum and energy after interacting with grains, which results in a decrease of both gas velocity and temperature. Consequently, this results in a significant change of dynamic pressure and a reduction in the number of eroded grain particles.

(6) It was discovered that the gas velocity and temperature of a two-way coupled model were smaller than those of a one-way coupled model, and a similar trend was also observed for the granular phase.

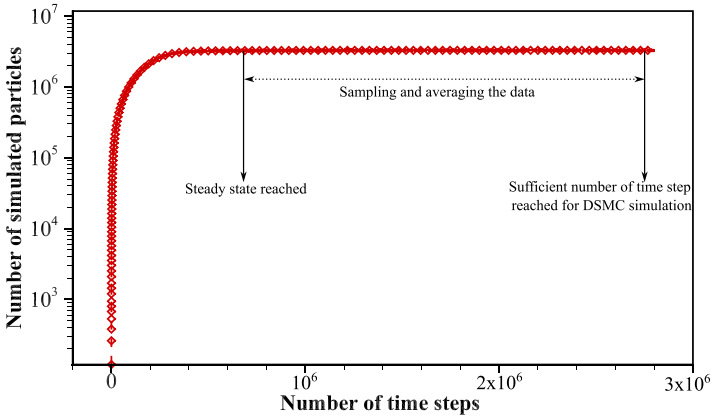

FIG. 27. Evolution of number of simulated gas particles in the domain.

(7) The coupling of the DSMC method with DEM was found to be helpful in a realistic modeling of grain-grain interactions. This framework allowed us to vary coefficients of restitution and friction, enabling a more detailed investigation of the problem.

The data that support the findings of this study are available from the corresponding author upon reasonable request.

ACKNOWLEDGMENTS

The authors acknowledge the financial support extended by the Science and Engineering Research Board (SERB) through Grant No. CRG/2019/003989 in performing this work. They also acknowledge the National Supercomputing Mission (NSM) for providing computing resources of "PARAM Sanganak" at IIT Kanpur, which is implemented by C-DAC and supported by the Ministry of Electronics and Information Technology (MeitY) and the Department of Science and Technology (DST), Government of India. A.B. is thankful to the Ministry of Education, Government of India for financial support through the Prime Minister Research Fellowship.

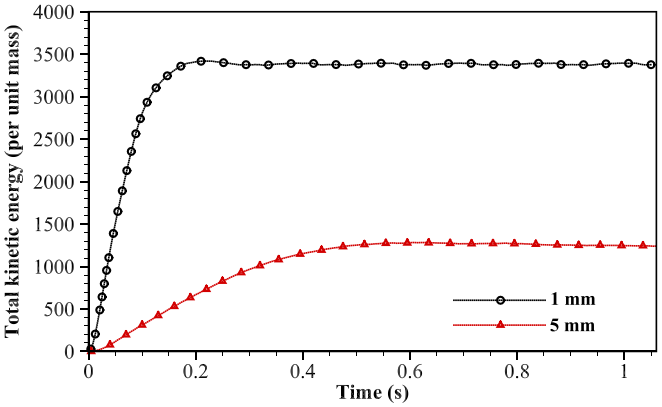

FIG. 28. Temporal variation of total kinetic energy of grains per unit mass.

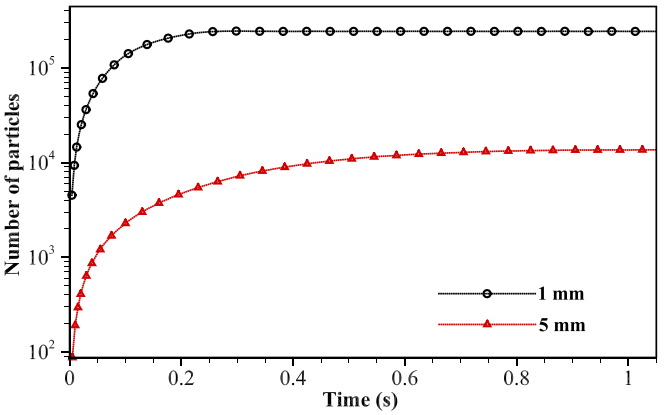

FIG. 29. Evolution of number of granular particles in the domain.

APPENDIX: CONVERGENCE OF THE SIMULATIONS

The convergence of numerical results is presented now. In Fig. 27 the convergence criterion for DSMC simulations is illustrated. The steady state is deemed to have been achieved once the number of simulated particles within the domain stabilizes. At this point, data samples are collected, and subsequently, the average of these sampled data is computed, marking the conclusion of the simulation subcycle. In Figs. 28 and 29, the convergence criteria for DEM subcycles are depicted for two representative grain sizes (1 mm and 5 mm). The attainment of a steady state in the DEM subcycles is indicated by two conditions: first, when the total kinetic energy of grain particles within the domain stabilizes, and second, when the number of grains within the domain reaches a stable value, indicating a balance between eroded particles and number of particles exiting the domain. Upon meeting these conditions, the DEM subcycles are considered converged, as demonstrated by Figs. 28 and 29.

[1] E. Grün, M. Horanyi, and Z. Sternovsky, The lunar dust environment, Planet. Space Sci. **59**, 1672 (2011).

[2] A. V. Zakharov, L. M. Zelenyi, and S. I. Popel, Lunar dust: Properties and potential hazards, Solar Syst. Res. **54**, 455 (2020).

[3] A. M. Korzun, C. J. Eberhart, J. West, P. Liever, A. Weaver, J. Mantovani, A. Langton, B. Kemmerer, and A. Atkins, Design of a subscale, inert gas test for plume-surface interactions in a reduced pressure environment, in *Proceedings of the AIAA SCITECH* (AIAA Press, Reston, VA, 2022).

[4] S. Singh, P. Chauhan, P. Roy, T. R. Martha, and I. C. Das, Characterisation of ejecta halo on the lunar surface around Chandrayaan-3 vikram lander using OHRC imagery, J. Indian Soc. Remote Sensing **51**, 1919 (2023) .

[5] L. Roberts, The action of a hypersonic jet on a dust layer, in *Institute Of Aerospace Sciences 31st Annual Meeting* (New York, NY, 1963), IAS Paper No. 63-50.

[6] R. E. Hutton, Comparison of soil erosion theory with scaled LM jet erosion tests, No. TRW-10608-6004-R0-00, 1968, https://ntrs.nasa.gov/citations/19690001354.

[7] P. T. Metzger, J. E. Lane, and C. D. Immer, Modification of Roberts' theory for rocket exhaust plumes eroding lunar soil, in *Earth & Space 2008: Engineering, Science, Construction, and Operations in Challenging Environments* (American Society of Civil Engineers, Reston, VA, 2008), pp. 1–8.

[8] N. S. Land and L. V. Clark, *Experimental Investigation of Jet Impingement on Surfaces of Fine Particles in a Vacuum Environment* (National Aeronautics and Space Administration, Washington, DC, 1965).

[9] J. D. Alexander, W. M. Roberds, and R. F. Scott, Soil erosion by landing rockets final report, Tech. Rep. 21 (1966).

[10] P. T. Metzger, C. D. Immer, C. M. Donahue, B. M. Vu, R. C. Latta III, and M. Deyo-Svendsen, Jet-induced cratering of a granular surface with application to lunar spaceports, J. Aerosp. Eng. **22**, 24 (2009).

[11] P. T. Metzger, J. Smith, and J. E. Lane, Phenomenology of soil erosion due to rocket exhaust on the moon and the Mauna Kea lunar test site, J. Geophys. Res. **116**, E06005 (2011).

[12] M. Kuhns, P. Metzger, A. Dove, J. Byron, S. Lamb, T. Roberson, L. Lohman, W. Chambers, G. Rixon, R. Kuhns *et al.*, Deep regolith cratering and plume effects modeling for lunar landing sites, in *Earth and Space 2021* (American Society of Civil Engineers, Reston, VA, 2021), pp. 62–78.

[13] L. Roberts, The interaction of a rocket exhaust with the lunar surface, Fluid Dyn. Asp. Space Flight **2**, 269 (1966).

[14] M. A. Gallis, J. R. Torczynski, and D. J. Rader, An approach for simulating the transport of spherical particles in a rarefied gas flow via the direct simulation Monte Carlo method, Phys. Fluids **13**, 3482 (2001).

[15] S. Gimelshein, A. Alexeenko, D. Wadsworth, and N. Gimelshein, The influence of particulates on thruster plume/shock layer interaction at high altitudes, in *Proceedings of the 43rd AIAA Aerospace Sciences Meeting and Exhibit* (AIAA Press, Reston, VA, 2004), p. 766.

[16] J. M. Burt, Monte Carlo simulation of solid rocket exhaust plumes at high altitude, Ph.D. thesis, University of Michigan (2006).

[17] F. Lumpkin, III, P. Stuart, and G. Le Beau, Enhanced analyses of plume impingement during Shuttle-Mir docking using a combined CFD and DSMC methodology, in *Proceedings of the 31st Thermophysics Conference* (1996), p. 1877.

[18] J. Marichalar, A. Prisbell, F. Lumpkin, and G. LeBeau, Study of plume impingement effects in the lunar lander environment, in *27th International Symposium on Rarefied Gas Dynamics*, AIP Conference Proceedings Vol. 1333 (American Institute of Physics, Melville, NY, 2011), pp. 589–594.

[19] J. E. Lane, P. T. Metzger, C. D. Immer, and X. Li, Lagrangian trajectory modeling of lunar dust particles, in *Proceedings of the Earth and Space 2008: Engineering, Science, Construction, and Operations in Challenging Environments* (American Society of Civil Engineers, Reston, VA, 2008), pp. 1–9.

[20] A. Tosh, P. A. Liever, R. R. Arslanbekov, and S. D. Habchi, Numerical analysis of spacecraft rocket plume impingement under lunar environment, J. Spacecr. Rockets **48**, 93 (2011).

[21] A. B. Morris, D. B. Goldstein, P. L. Varghese, and L. M. Trafton, Plume impingement on a dusty lunar surface, in *27th International Symposium on Rarefied Gas Dynamics*, AIP Conference Proceedings Vol. 1333 (American Institute of Physics, Melville, NY, 2011), pp. 1187–1192.

[22] A. B. Morris, D. B. Goldstein, P. L. Varghese, and L. M. Trafton, Modeling the interaction between a rocket plume, scoured regolith, and a plume deflection fence, in *Proceedings of the Thirteenth ASCE Aerospace Division Conference on Engineering, Science, Construction, and Operations in Challenging Environments, and the 5th NASA/ASCE Workshop on Granular Materials in Space Exploration* (American Society of Civil Engineers, Reston, VA, 2012), pp. 189–198.

[23] A. B. Morris, D. B. Goldstein, P. L. Varghese, and L. M. Trafton, Approach for modeling rocket plume impingement and dust dispersal on the moon, J. Spacecr. Rockets **52**, 362 (2015).

[24] A. B. Morris, Simulation of Rocket Plume Impingement and Dust Dispersal on the Lunar Surface, Ph.D. Dissertation, University of Texas, Austin, TX, USA (2012).

[25] C. White, T. J. Scanlon, J. A. Merrifield, K. Kontis, T. Langener, and J. Alves, Numerical and experimental capabilities for studying rocket plume-regolith interactions, in *30th International Symposium on Rarefied Gas Dynamics: RGD*, AIP Conference Proceedings Vol. 1786 (AIP Publishing, Melville, NY, 2016), p. 170003.

[26] J. Burt and I. Boyd, Development of a two-way coupled model for two phase rarefied flows, in *Proceedings of the 42nd AIAA Aerospace Sciences Meeting and Exhibit* (AIAA Press, Reston, VA, 2004), p. 1351.

[27] A. B. Morris, D. B. Goldstein, P. L. Varghese, and L. M. Trafton, Far field deposition of scoured regolith resulting from lunar landings, in *28th International Symposium on Rarefied Gas Dynamics*, AIP Conference Proceedings Vol. 1501 (American Institute of Physics, Melville, NY, 2012), pp. 1220–1227.

[28] X. He, B. He, and G. Cai, Simulation of rocket plume and lunar dust using DSMC method, Acta Astronaut. **70**, 100 (2012).

[29] K. J. Berger, A. Anand, P. T. Metzger, and C. M. Hrenya, Role of collisions in erosion of regolith during a lunar landing, Phys. Rev. E **87**, 022205 (2013).
[30] M. Gale, R. S. Mehta, P. Liever, J. Curtis, and J. Yang, Realistic regolith models for plume-surface interaction in spacecraft propulsive landings, in *Proceedings of the AIAA Scitech 2020 Forum* (AIAA Press, Reston, VA, 2020).
[31] T. R. Yeager, D. H. Fontes, P. Metzger, and M. P. Kinzel, Numerical model of jet impingement and particle trajectories in extraterrestrial landing events using an Euler-Lagrange method, in *Proceedings of the AIAA Scitech 2020 Forum* (AIAA Press, Reston, VA, 2020).
[32] A. K. Chinnappan, R. Kumar, and V. K. Arghode, Modeling of dusty gas flows due to plume impingement on a lunar surface, Phys. Fluids **33**, 053307 (2021).
[33] M. B. Agir, C. White, and K. Kontis, The effect of increasing rarefaction on the formation of Edney shock interaction patterns: Type-I to type-VI, Shock Waves **32**, 733 (2022).
[34] Z. Cao, M. B. Agir, C. White, and K. Kontis, An open source code for two-phase rarefied flows: RarefiedMultiphaseFoam, Comput. Phys. Commun. **276**, 108339 (2022).
[35] Z. Cao, C. White, M. B. Agir, and K. Kontis, Lunar plume-surface interactions using rarefiedMultiphase-Foam, Front. Mech. Eng. **9**, 1116330 (2023).
[36] H. Zhang, C. Li, J. You, X. Zhang, Y. Wang, L. Chen, Q. Fu, B. Zhang, and Y. Wang, The investigation of plume-regolith interaction and dust dispersal during Chang'e-5 descent stage, Aerospace **9**, 358 (2022).
[37] M. Mehta, A. Sengupta, N. O. Renno, J. W. Van Norman, P. G. Huseman, D. S. Gulick, and M. Pokora, Thruster plume surface interactions: Applications for spacecraft landings on planetary bodies, AIAA J. **51**, 2800 (2013).
[38] A. Sengupta, J. Kulleck, S. Sell, J. Van Norman, M. Mehta, and M. Pokora, Mars lander engine plume impingement environment of the mars science laboratory, in *Proceedings of the 2009 IEEE Aerospace Conference* (IEEE, New York, 2009), pp. 1–10.
[39] K. Balakrishnan and J. Bellan, High-fidelity modeling and numerical simulation of cratering induced by the interaction of a supersonic jet with a granular bed of solid particles, Int. J. Multiphase Flow **99**, 1 (2018).
[40] K. Balakrishnan and J. Bellan, A multi-species modeling framework for describing supersonic jet-induced cratering in a granular bed: Cratering on Titan case study, Int. J. Multiphase Flow **118**, 205 (2019).
[41] K. Balakrishnan and J. Bellan, Fluid density effects in supersonic jet-induced cratering in a granular bed on a planetary body having an atmosphere in the continuum regime, J. Fluid Mech. **915**, A29 (2021).
[42] A. Rahimi, O. Ejtehadi, K. H. Lee, and R. S. Myong, Near-field plume-surface interaction and regolith erosion and dispersal during the lunar landing, Acta Astronaut. **175**, 308 (2020).
[43] O. Ejtehadi, A. Rahimi, A. Karchani, and R. S. Myong, Complex wave patterns in dilute gas–particle flows based on a novel discontinuous Galerkin scheme, Int. J. Multiphase Flow **104**, 125 (2018).
[44] G. Shallcross, Modeling particle-laden compressible flows with an application to plume-surface interactions, Ph.D. thesis, University of Michigan, Ann Arbor (2021).
[45] S. Schaaf and P. Chambre, Flow of rarefied gases, high speed aerodynamics and jet propulsion, in *Fundamentals of Gas Dynamics* (Princeton University Press, Princeton, NJ, 1958), Vol. 3, pp. 687–741.
[46] G. A. Bird, *Molecular Gas Dynamics and the Direct Simulation of Gas Flowss* (Oxford University Press, New York, 1994).
[47] J. F. Padilla and I. D. Boyd, Assessment of gas-surface interaction models for computation of rarefied hypersonic flow, J. Thermophys. Heat Transfer **23**, 96 (2009).
[48] J. C. Maxwell, VII, On stresses in rarified gases arising from inequalities of temperature, Philos. Trans. R. Soc. London **170**, 231 (1879).
[49] R. Kumar and A. K. Chinnappan, Development of a multi-species, parallel, 3D direct simulation Monte-Carlo solver for rarefied gas flows, Comput. Fluids **159**, 204 (2017).
[50] A. K. Chinnappan and R. Kumar, Modeling of high speed gas-granular flow over a 2D cylinder in the direct simulation Monte-Carlo framework, Granular Matter **18**, 35 (2016).
[51] J. Shäfer, S. Dippel, and D. E. Wolf, Force schemes in simulations of granular materials, J. Phys. I France **6**, 5 (1996).

[52] B. K. Mishra, A review of computer simulation of tumbling mills by the discrete element method: Part I—Contact mechanics, Int. J. Miner. Process. **71**, 73 (2003).
[53] T. Pöschel and T. Schwager, *Computational Granular Dynamics: Models and Algorithms* (Springer Science & Business Media, Berlin, Heidelberg, 2005).
[54] P. A. Cundall and O. D. L. Strack, A discrete numerical model for granular assemblies, Geotechnique **29**, 47 (1979).
[55] H. Kruggel-Emden, M. Sturm, S. Wirtz, and V. Scherer, Selection of an appropriate time integration scheme for the discrete element method (DEM), Comput. Chem. Eng. **32**, 2263 (2008).
[56] A. Bhateja, I. Sharma, and J. K. Singh, Scaling of granular temperature in vibro-fluidized grains, Phys. Fluids **28**, 043301 (2016).
[57] L. E. Silbert, D. Ertaş, G. S. Grest, T. C. Halsey, D. Levine, and S. J. Plimpton, Granular flow down an inclined plane: Bagnold scaling and rheology, Phys. Rev. E **64**, 051302 (2001).
[58] A. K. Chinnappan, R. Kumar, V. K. Arghode, and R. S. Myong, Transport dynamics of an ellipsoidal particle in free molecular gas flow regime, Phys. Fluids **31**, 037104 (2019).
[59] C. T. Crowe, J. D. Schwarzkopf, M. Sommerfeld, and Y. Tsuji, *Multiphase Flows with Droplets and Particles* (CRC Press, Boca Raton, 2011).
[60] R. Kumar, Z. Li, A. Van Duin, and D. Levin, Molecular dynamics studies to understand the mechanism of heat accommodation in homogeneous condensing flow of carbon dioxide, J. Chem. Phys. **135**, 064503 (2011).
[61] F. E. Marble, Dynamics of dusty gases, Annu. Rev. Fluid Mech. **2**, 397 (1970).
[62] P. A. Chambre and S. A. Schaaf, *Flow of Farefied Gases*, High Speed Aerodynamics and Jet Propulsion series Vol. 4971 (Princeton University Press, Princeton, NJ, 2017).
[63] A. K. Oppenheim, Generalized theory of convective heat transfer in a free-molecule flow, J. Aeronaut. Sci. **20**, 49 (1953).
[64] F. M. Sauer, Convective heat transfer from spheres in a free-molecule flow, J. Aeronaut. Sci. **18**, 353 (1951).
[65] C. Immer, J. Lane, P. Metzger, and S. Clements, Apollo video photogrammetry estimation of plume impingement effects, Icarus **214**, 46 (2011).
[66] L. Roberts, The interface of a rocket exhaust with the lunar surface, in *The Fluid Dynamic Aspects of Space Flight* (1966), pp. 269–290.
[67] P. T. Metzger, J. E. Lane, C. D. Immer, J. N. Gamsky, W. Hauslein, X. Li, R. C. Latta, III, and C. M. Donaue, Scaling of erosion rate in subsonic jet experiments and apollo lunar module landings, in *Proceedings of the Earth and Space 2010: Engineering, Science, Construction, and Operations in Challenging Environments* (American Society of Civil Engineers, Reston, VA, 2010), pp. 191–207.
[68] J. E. Lane and P. T. Metzger, Estimation of Apollo lunar dust transport using optical extinction measurements, Acta Geophys. **63**, 568 (2015).
[69] W. D. Carrier III, Particle size distribution of lunar soil, J. Geotech. Geoenviron. Eng. **129**, 956 (2003).
[70] W. R. Hammock Jr, E. C. Currie, and A. E. Fisher, Apollo experience report: Descent propulsion system, Technical Note D-7143 (1973), https://ntrs.nasa.gov/citations/19730011150.
[71] P. Metzger, X. Li, C. Immer, and J. Lane, ISRU implications for lunar and Martian plume effects, in *Proceedings of the 47th AIAA Aerospace Sciences Meeting including The New Horizons Forum and Aerospace Exposition* (AIAA Press, Reston, VA, 2009), p. 1204.